e-ISSN 2150-5551
CN 31-2103/TB

Nano-Micro Letters

REVIEW

https://doi.org/10.1007/s40820-024-01441-1

New-Generation Ferroelectric AlScN Materials

Yalong Zhang[1], Qiuxiang Zhu[1] ✉, Bobo Tian[1] ✉, Chungang Duan[1,2]

Cite as
Nano-Micro Lett.
(2024) 16:227

Received: 14 March 2024
Accepted: 6 May 2024
© The Author(s) 2024

HIGHLIGHTS

- Ferroelectricity and domain dynamics of emerging ferroelectric AlScN films were discussed.
- The performance optimization of ferroelectric AlScN films grown by different deposition techniques was comprehensively analyzed.
- The challenges and perspectives regarding the commercial avenue of AlScN-based memories and in-memory computing applications were summarized.

ABSTRACT Ferroelectrics have great potential in the field of nonvolatile memory due to programmable polarization states by external electric field in nonvolatile manner. However, complementary metal oxide semiconductor compatibility and uniformity of ferroelectric performance after size scaling have always been two thorny issues hindering practical application of ferroelectric memory devices. The emerging ferroelectricity of wurtzite structure nitride offers opportunities to circumvent the dilemma. This review covers the mechanism of ferroelectricity and domain dynamics in ferroelectric AlScN films. The performance optimization of AlScN films grown by different techniques is summarized and their applications for memories and emerging in-memory computing are illustrated. Finally, the challenges and perspectives regarding the commercial avenue of ferroelectric AlScN are discussed.

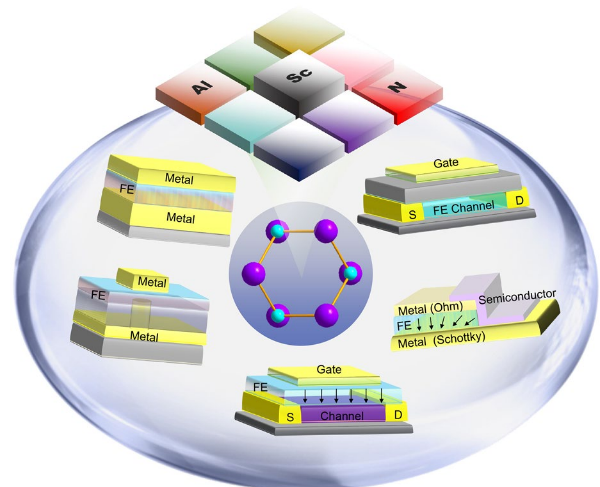

KEYWORDS AlScN; Ferroelectrics; Nonvolatile memory; In-memory computing

✉ Qiuxiang Zhu, qxzhu@clpm.ecnu.edu.cn; Bobo Tian, bbtian@ee.ecnu.edu.cn
[1] Key Laboratory of Polar Materials and Devices, Ministry of Education, Shanghai Center of Brain-Inspired Intelligent Materials and Devices, Department of Electronics, East China Normal University, Shanghai 200241, People's Republic of China
[2] Collaborative Innovation Center of Extreme Optics, Shanxi University, Taiyuan 030006, Shanxi, People's Republic of China

Published online: 25 June 2024

Shanghai Jiao Tong University Press

Springer

1 Introduction

In the era of big data, artificial intelligence (AI) has made breakthroughs in the application of facial recognition, driverless driving, intelligent robots and other fields. At present, the implementation of AI is mainly based on algorithms, which require chips with large computational power for data processing. The computational power of the chip and the development of AI are complementary to each other [1–5]. The separation of the central processing unit (CPU) and memory in traditional von Neumann architecture causes latency and energy consumption during data transfer (Fig. 1a) [6, 7]. Furthermore, although CPU performance (ns level processing) has been greatly improved with the development of integrated circuit technology, the low access speed (μs level) of memory leads to severe time consumption and limits the whole performance [8–11]. In order to break through these bottlenecks, NVIDIA's multi-core graphic processing unit (GPU) and Google's tensor processing unit (TPU) with a processing near memory architecture, and in-memory computing (IMC) technology based on nonvolatile memory (NVM) have emerged in recent years (Fig. 1b) [12, 13]. In-memory computing within artificial neural networks enables highly efficient data-intensive computation due to the elimination of data migration and access. The vector–matrix multiplication (VMM) is a key operation in artificial neural networks. The crossbar array constructed with NVMs can perform VMM operation in one step following circuit laws [14]. The programmable conductance matrix is multiplied by the inputing voltage vector applied at the input wordlines in parallel to obtain current based on Ohm's law, and the accumulated current at each bitline obeys Kirchhoff's current law. Thanks to the science and

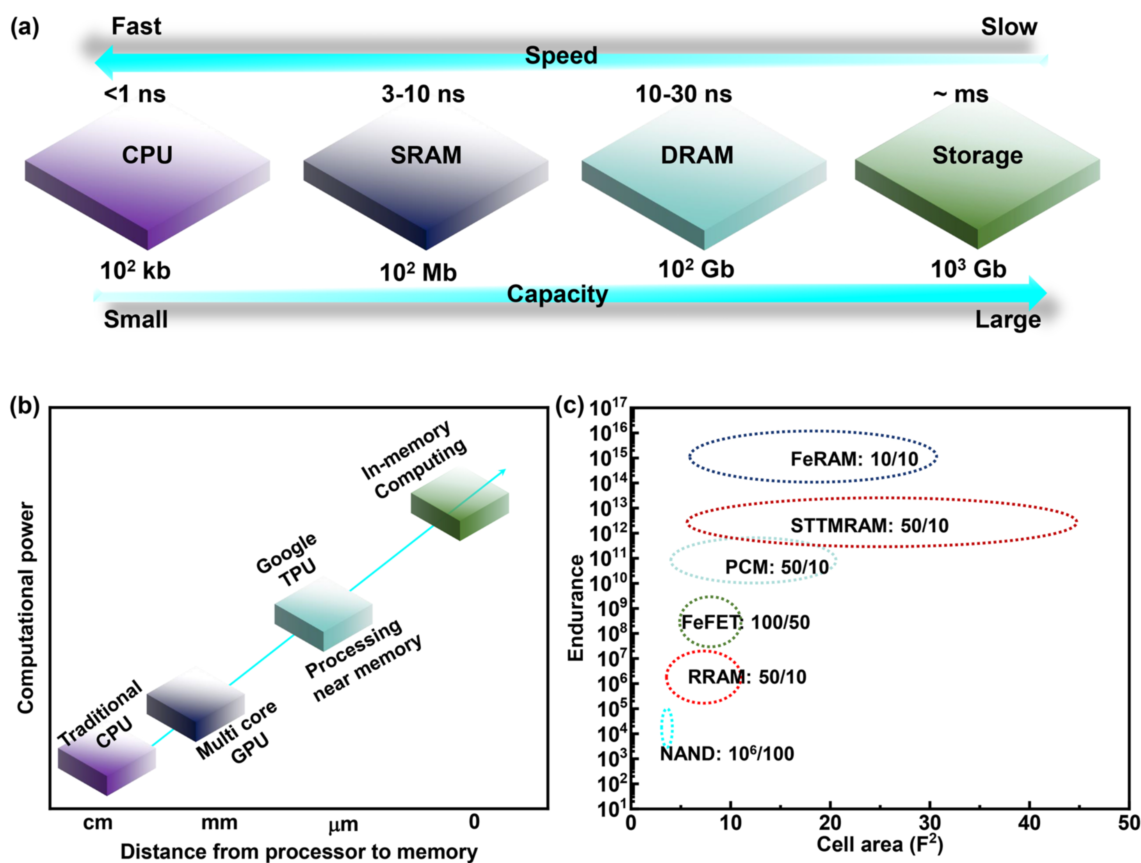

Fig. 1 **a** Memory and CPU in von Neumann architecture. **b** The technical roadmap to improving computing efficiency. **c** The performance comparison of existing NVM. Here, "FeRAM:10/10" means that the read/write time of FeRAM is 10/10 ns, and the remaining definitions follow similar rules. Data are obtained from Ref. [19–24]

© The authors
https://doi.org/10.1007/s40820-024-01441-1

technology advancement, a large number of NVMs emerge, including NAND flash, resistive random-access memory (RRAM), magneto-resistive RAM (MRAM), phase change RAM (PCRAM) and ferroelectric memory (FeM) [15–18]. Among them, FeM devices have unique superiorities with respect to power consumption, operation speed and endurance (Fig. 1c). For example, ferroelectric RAM (FeRAM) has faster read/write speeds and better endurance than other RAMs, and the read/write speed and endurance of ferroelectric field effect transistors (FeFETs) are also better than commercially available NAND flash. However, as will be discussed below, there is still space for the cell size of FeMs to shrink, thereby facilitating higher integration density.

Ferroelectric materials have spontaneous polarization that is switchable by electric field. Notably, multiple stable polarization states can be configurated by precisely controlling the parameters of electric field (e.g., amplitude, frequency and duration) [25–28]. It should be noted that the ferroelectric polarization states are regulated by the electric field, which avoids joule heating caused by current and significantly reduces energy consumption. The fast speed and low energy cost of polarization switching allow a high computational power of FeMs. For instance, the ferroelectric tunnel junction (FTJ) array has been reported to reach 100 tera-operations per second per watt [29]. An ideal FeM demands the involved ferroelectric materials to possess the following characteristics: (1) Good CMOS compatibility [30–32]. (2) Suitable remanent polarization (P_r) to achieve more bits memory [33, 34]. (3) Optimized coercive electric field (E_c) for long-term retention and large memory

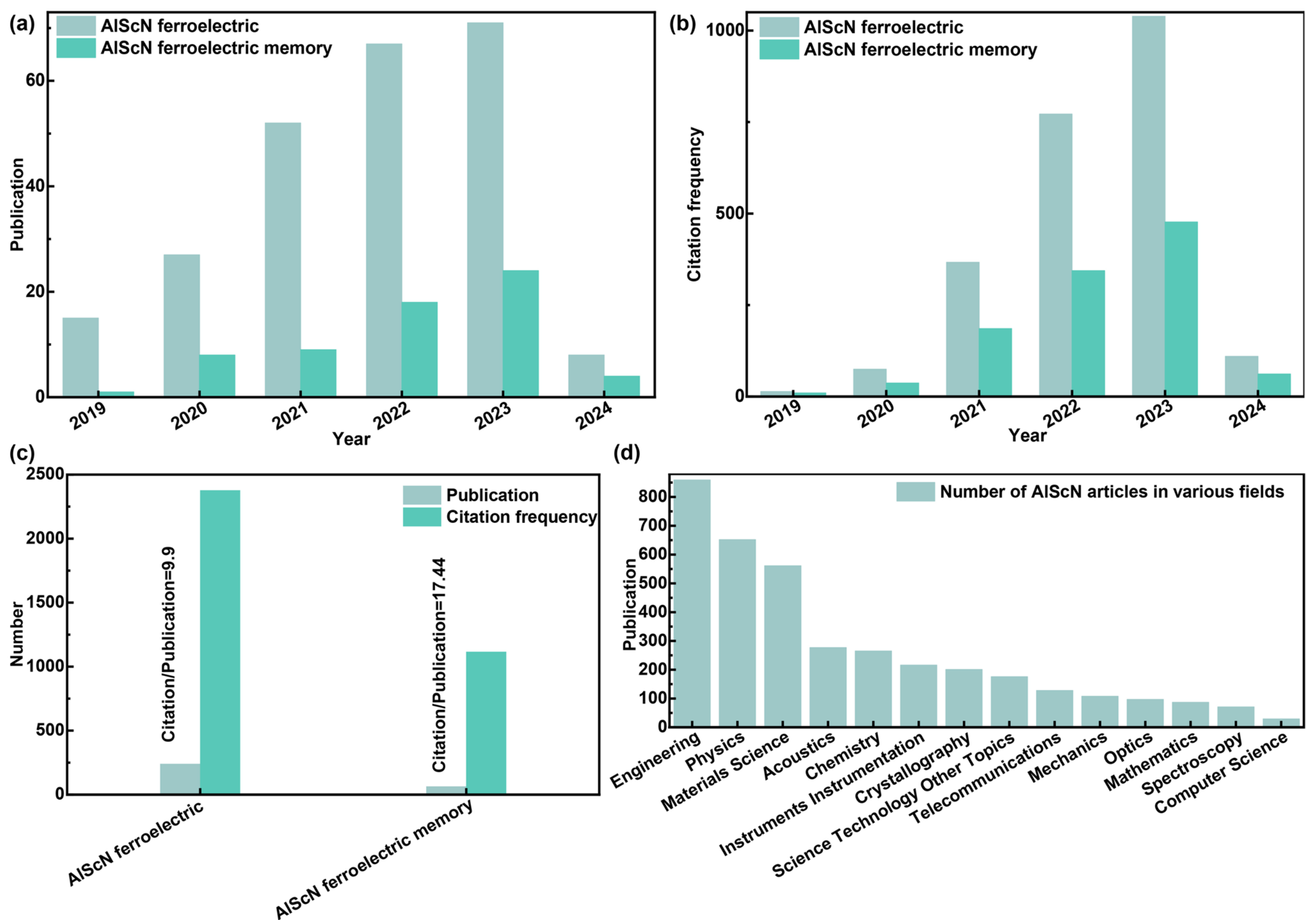

Fig. 2 Retrieved data from Web of Science. **a** Publication, **b** citation frequency and **c** citation frequency/publication ratio of AlScN, AlScN ferroelectricity and AlScN ferroelectric memory. **d** The publication of AlScN in various research areas. Searching keywords [AlScN ferroelectric: (aluminum scandium nitride/scandium aluminum nitride/Sc-doped aluminum nitride/AlScN/ScAlN) ferroelectric; AlScN ferroelectric memory: (aluminum scandium nitride/scandium aluminum nitride/Sc-doped aluminum nitride/AlScN/ScAlN) ferroelectric memory]

window, as well as excellent endurance and low operation voltage [35–37]. (4) Stable ferroelectric phase ensures the high device-to-device uniformity. Few ferroelectric materials except wurtzite-structured nitrides (e.g., AlScN, AlBN, GaScN) [38] and oxides (e.g., ZnMgO) [39], meet all above requirements simultaneously. Ferroelectricity discovered in AlScN films since 2019 brings new prosperity into FeM [40].

Despite the fact that the number of articles about AlScN-based FeM has increased significantly with an average number of citations per article up to 17.44 since the first report of AlScN-based ferroelectric in 2019 (Fig. 2), the review article on the topic of AlScN-based FeM is rare. Therefore, it is necessary to systematically review the conspicuous and booming progresses of AlScN-based FeM. This review summarizes the latest advances in AlScN-based FeM. Chapter 2 reviews the development history of ferroelectrics and FeM. In chapter 3, the ferroelectric mechanism and domain dynamics of AlScN are discussed, and the performance optimization of AlScN thin films by various deposition methods is summarized. Chapter 4 provides an overview of AlScN-based FeM and its application in the field of IMC. In chapter 5, the challenges and perspectives of ferroelectric AlScN are discussed. This review will play a role of guiding

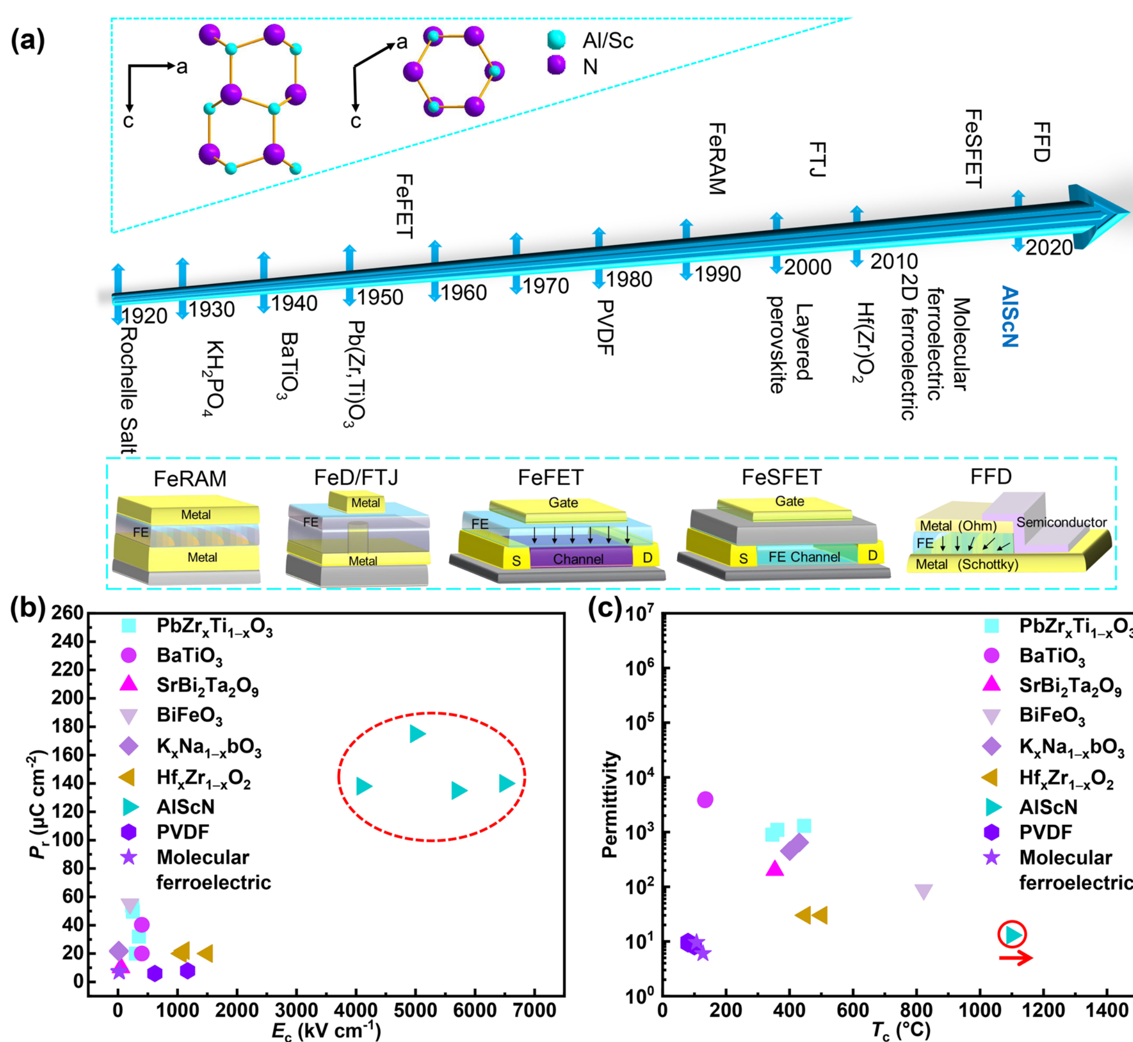

Fig. 3 **a** Development history of ferroelectric materials and FeM. The top illustration shows the crystal structure of AlScN, and the bottom illustration exhibits the structure of FeM, wherein FeSFET, FeD and FFD represent ferroelectric–semiconductor FET, ferroelectric diode and ferroelectric fin diode, respectively. **b** Comparison of P_r and E_c between AlScN and other common ferroelectrics. **c** Comparison of permittivity and T_c among different ferroelectrics. $PbZr_xTi_{1-x}O_3$ [41–46], $BaTiO_3$ [47–49], $SrBi_2Ta_2O_9$ [50], $BiFeO_3$ [51–53], $K_xNa_{1-x}NbO_3$ [54, 55], $Hf_xZr_{1-x}O_2$ [56–58], AlScN [59–62], PVDF [63–66], molecular ferroelectric [67, 68]

© The authors

the future development of AlScN-based memory and neuromorphic devices.

2 History of Ferroelectric Materials and FeM

It has been 104 years since ferroelectricity was first discovered in Rochelle salt in 1920 (Fig. 3a) [69]. Essentially, Rochelle salt was the first molecular ferroelectric crystal, but the concept of molecular ferroelectrics was proposed by Xiong et al. in the 2010s [70]. KH_2PO_4 was found to be ferroelectric in 1933, but it was soluble in water like Rochelle salt [71]. It was not until the 1940s that the emergence of $BaTiO_3$ (BTO) and $PbZr_xTi_{1-x}O_3$ (PZT) provided the basis for the research of FeM [22, 72, 73]. In 1980, ferroelectricity was discovered in the copolymer of vinylidene fluoride and trifluoroethylene (P(VDF-TrFE)), and subsequently, poly(vinylidene fluoride) (PVDF)-based ternary and quaternary copolymers were derived. Ferroelectric polymers are widely used in wearable devices due to their good flexibility [74]. The concept of FeM was first proposed in 1952 [75], and the first commercial FeRAM based on PZT was manufactured in 1990 [76]. Immediately afterward, RAMTRON (1993), Samsung (1996) and Panasonic released their FeRAM products. However, perovskite-type ferroelectric materials are incompatible with CMOS back-end-of-line (BEOL) [77], and their performance seriously deteriorates at 130 nm or smaller process node [78, 79]. $SrBi_2Ta_2O_9$ was used as a substitute of PZT to prepare FeRAM and its FeFETs was demonstrated, but weak oxygen binding made its performance slowly fade away [50].

Compared with the commercial development of FeRAM in the business community, other FeMs are still undergoing laboratory research. The concept of FTJ was first proposed in 1971 [80], but the requirement for high-quality ultra-thin ferroelectric films in FTJ prevented its realization until three decades later [81]. Its nondestructive conductance read mode and simple structure of FTJ are appealing for high-density memory and IMC applications. On the other hand, the poor endurance issue (usually $< 10^4$) due to the ultra-thin thickness for direct quantum tunneling hinders its commercialization. The following ferroelectric diode (FD) and new-emerging ferroelectric fin diode (FFD) provide avenues to overcome the direct-tunneling limitation of FTJ memory [27]. In FFD, a ferroelectric capacitor and a fin-like semiconductor channel are combined to share both top and bottom electrodes. The intended Schottky barrier at one of semiconductor–electrode interfaces renders lateral field on the vertical semiconductor channel, resulting in ferroelectric domains-dominated resistive switching. The thickness of the ferroelectric defined by channel length does not suffer the direct quantum tunneling limit, avoiding the endurance issue in FTJ.

The prototype of FeFETs was initially proposed in the mid-1950s, which utilizes ferroelectric polarization to regulate the conductance of the semiconductor channel [82]. In 1974, Sugibuchi et al. prepared a metal–ferroelectric–semiconductor (MFS)-structured FeFETs, employing bismuth titanate as the ferroelectric layer and silicon as the channel [83]. It is noteworthy that the charge injection from silicon into the ferroelectric layer impacts the device performance [84]. To address this issue, Kijima et al. introduced SiO_2 between Si and ferroelectric layer, creating a metal–ferroelectric–insulator–semiconductor (MFIS) structure [85]. However, SiO_2, with low permittivity, tends to dissipate more voltage and cause breakdown, prompting the substitution of SiO_2 with HfO_2, which has higher permittivity [86]. Nevertheless, the poor interface quality of ferroelectric materials due to lattice mismatch between HfO_2 and perovskite ferroelectric layers remains significant challenge. The emergence of two-dimensional (2D) ferroelectric semiconductors has led to the proposal of a ferroelectric–semiconductor field-effect transistor memory (FeSFET), aimed at addressing the interface issue [87].

In 2011, silicon-doped HfO_2 was demonstrated to be ferroelectric [88]. HfO_2-based ferroelectrics can have high E_c and P_r at ultra-thin scale (below 5 nm) and is compatible with CMOS process [88, 89]. Immediately afterward, HfO_2-based FeFETs [90], FTJ [91] and FeRAM [92] were demonstrated one after another. In 2023, Yang et al. demonstrated a 9-Mb HZO-based FeRAM with 10^{12} cycle endurance [93]. However, the formation of metastable ferroelectric phase in HfO_2-based materials requires additional post-annealing treatment, tensile stress and the presence of oxygen vacancies [94, 95]. The competition among different crystalline phases always leads to polymorphisms [96, 97], which leads to uneven performance over small area of thin film [98], and poses a problem for massively integrated circuits. Therefore, there is an urgent need for alternative ferroelectric materials.

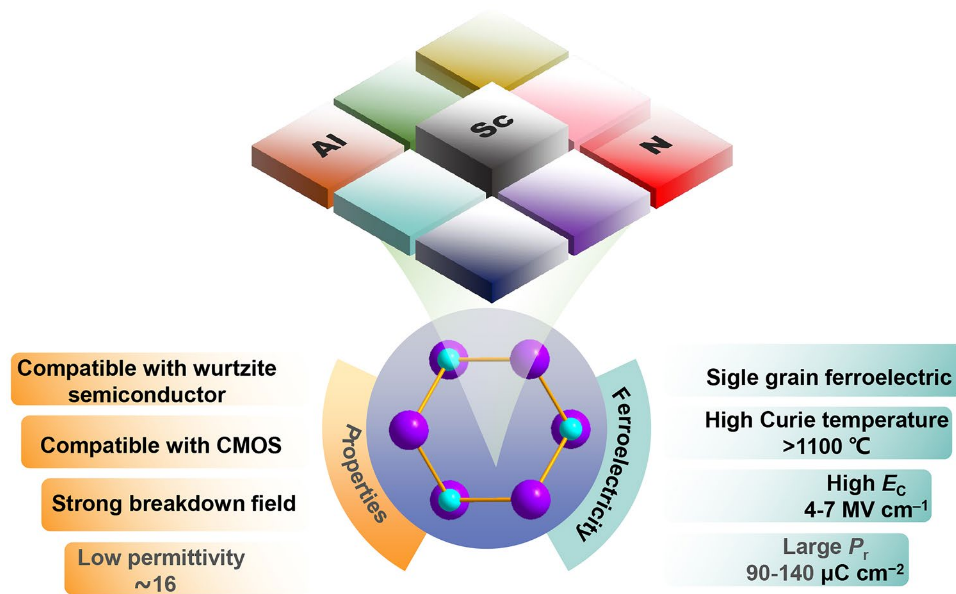

Fig. 4 Physical properties of ferroelectric AlScN

In 2019, Simon et al. demonstrated ferroelectricity in AlScN [99], and its polar wurtzite phase had the lowest thermodynamic energy [100], ensuring uniform ferroelectric performance at nanoscales. It is worth mentioning that AlScN has several times larger P_r and E_c value compared with traditional ferroelectric materials (Fig. 3b). The P_r and E_c of 10 nm AlScN film reached 100 μC cm^{-2} and 11.1 MV cm^{-1}, respectively [101]. The ferroelectricity of AlScN remains stable at 1100 °C [61], making it potential for applications in aerospace and other high-temperature environments (Fig. 3c) [102]. In addition, AlScN has the lowest permittivity among known inorganic ferroelectric materials [103]. A low-permittivity ferroelectric layer can reduce the voltage sharing of non-ferroelectric layers, beneficial for increasing the sensing margin of FeRAM. In addition, ultra-thin AlScN film with thickness of 5 nm still has ferroelectricity [104, 105]. Schönweger et al. reported that the switching voltage of sub-5 nm AlScN was reduced to 1 V [106], enabling AlScN-based ferroelectric NVM devices to be operated by low voltage [107]. AlScN can be grown using magnetron sputtering technology below 400 °C, ensuring compatibility with CMOS manufacturing processes. The lack of volatile elements in AlScN mitigates the risk of any detrimental contamination during the COMS process [108]. In summary, AlScN is the first ferroelectric material with all following merits of stable-phase ferroelectricity, CMOS BEOL compatibility, third-generation semiconductor compatibility and sustainable scaling, etc., and has broad prospects for commercial applications (Fig. 4) [109].

3 Ferroelectricity of AlScN

In order to understand the ferroelectricity of AlScN, this section will start with the crystal structures of ScN and AlN, and then introduce the relationship between ScN and AlN. Next, it will introduce the origin of AlScN's ferroelectricity, the influence of in-plane stress on AlScN's ferroelectricity due to the Sc doping, the temperature and film thickness dependence of AlScN's ferroelectricity, and the domain switching dynamics of AlScN.

3.1 Origin of Ferroelectricity of AlScN

In common sense, ScN has stable nonpolar rock salt structure, which is difficult to connect with wurtzite AlN. However, Farrer et al. predicted existence of metastable hexagonal ScN with nearly five-times coordination through local-density approximation (LDA) calculations [110]. Subsequently, Ranjan et al. conducted LDA calculations to predict the structural phase transition of hexagonal ScN from nonpolar to polar under continuous compressive strain [111].

© The authors https://doi.org/10.1007/s40820-024-01441-1

The above prediction of hexagonal ScN provides a prerequisite for the birth of ferroelectric Sc–Al–N in the future.

AlN with wurtzite structure (space group $P6_3mc$) has polarization along [001] direction, arising from the separation of Al^{3+} cation and N^{3-} anion centers [112, 113]. Therefore, there are two antiparallel polarization directions: N-polar and Al-polar [114]. Pure AlN is piezoelectric rather than ferroelectric material, because polarization cannot be switched by an electric field lower than dielectric breakdown limit [115, 116]. In other words, the polarization of wurtzite AlN would be switchable if reducing the energy barrier between the two polarization states.

Owing to the ultra-high thermal stability of wurtzite AlN, it is difficult to directly study the phase transition process as a function of temperature [60]. However, the pressure-induced phase transition process in AlN will bring some new ideas [117]. Vollstädt et al. demonstrated the phase transition from wurtzite to rock salt structure at 14–22 GPa [118]. Zagorac et al. predicted the first-order phase transition of AlN from wurtzite to rock salt at a pressure of 19 GPa [119]. Regarding the phase transition path of AlN from wurtzite to rock salt, most scholars support the view that layered hexagonal phase serving as an intermediate phase is energetically favorable [120, 121].

Tasnádi et al. revealed that Sc doping can flatten the energy landscape of AlN [122]. Wang et al. predicted that the ferroelectric switching barrier of AlScN decreased with the increase in Sc content, enabling the switching between Al-polar and N-polar in AlScN [123]. Zhang et al. speculated that AlScN shows stable polar wurtzite phase when Sc content is lower than 0.56, and nonpolar rock salt phase when Sc content is higher than 0.56 [116]. The ferroelectricity of AlScN is suggested to be related to the existence of metastable layered hexagonal phase of ScN (space group $P6_3/mmc$) [99], which plays the role of the transition state between the two polarization orientations of wurtzite structure to reduce the energy barrier between two polarization states (Fig. 5) [110].

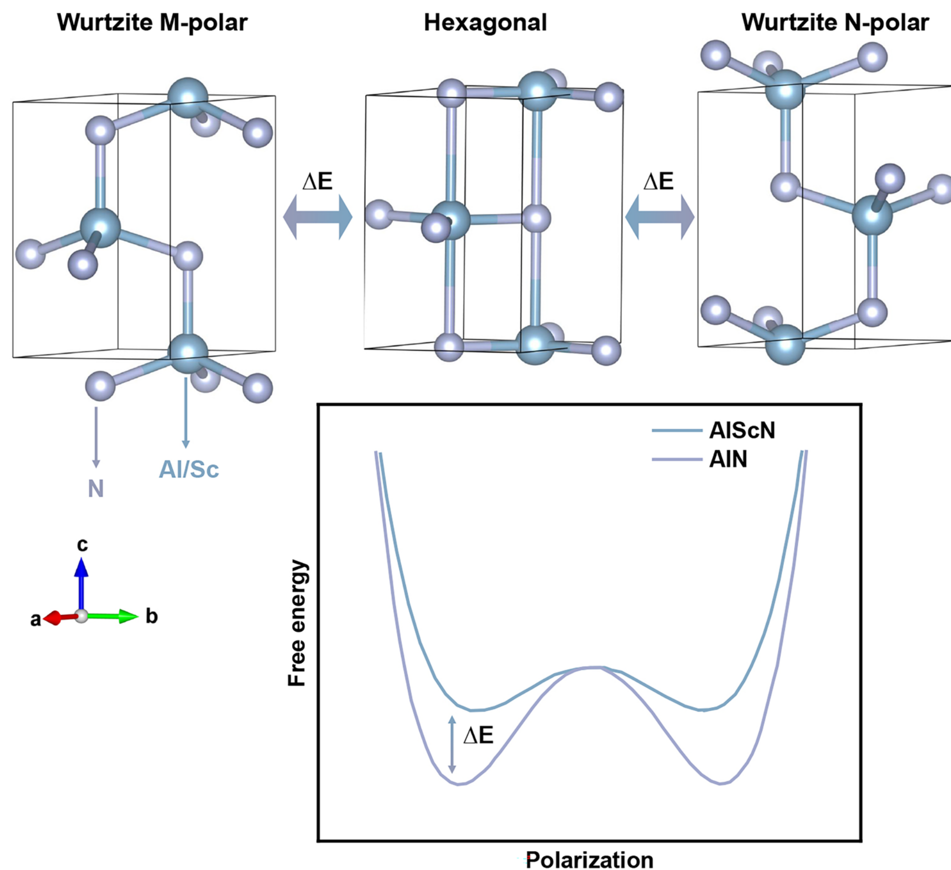

Fig. 5 Polarization switching process of AlScN and the change of double-well potential after Sc doping

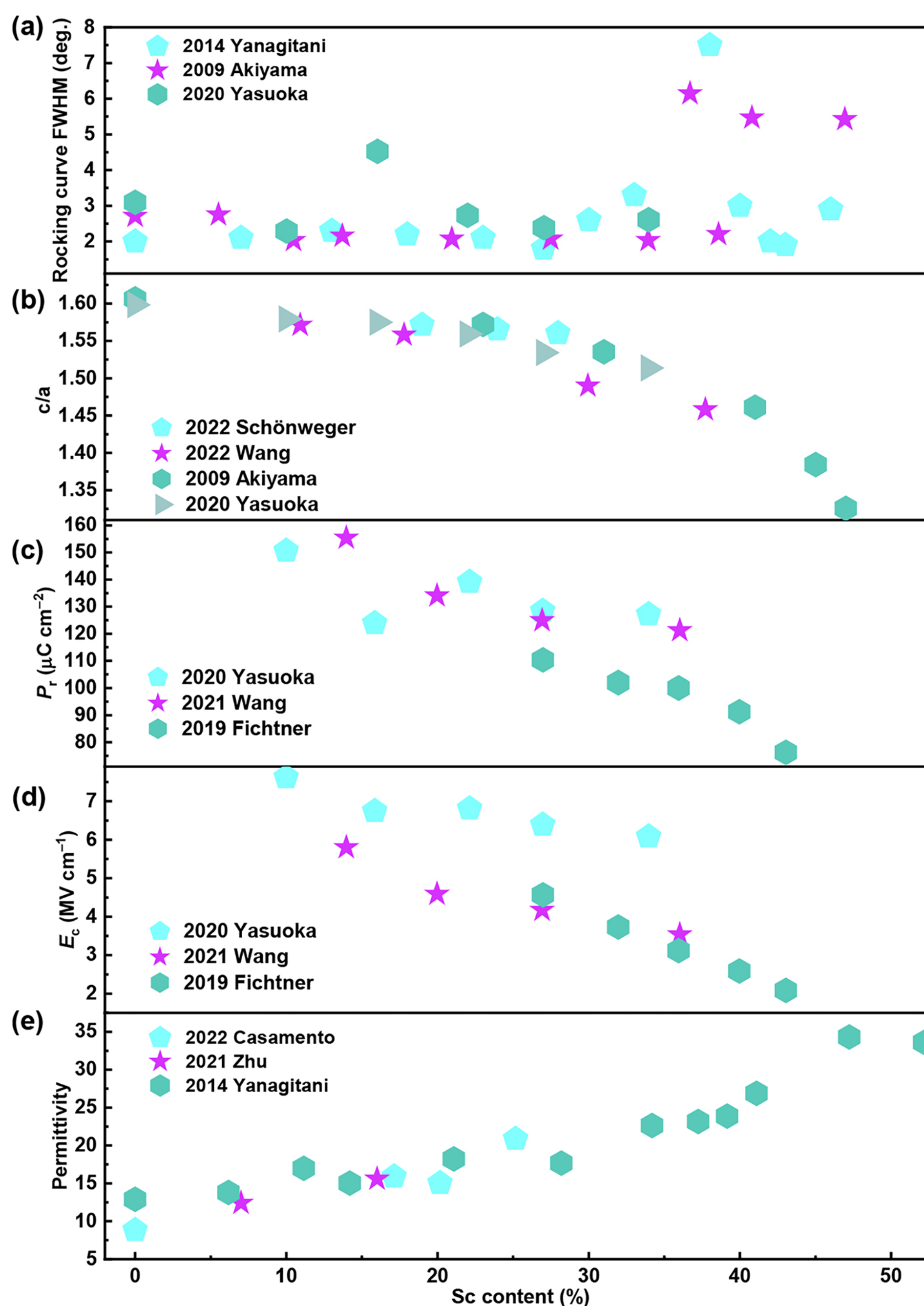

Fig. 6 Material properties of $Al_{1-x}Sc_xN$ as a function of the Sc concentration. **a** Rocking curve FWHM, **b** *c*/*a*, **c** P_r, **d** E_c and **e** permittivity. Data from Ref. [59, 99, 103, 124–129]

3.2 Factors Affecting the Ferroelectricity of AlScN

Despite theoretical predictions as a guide, it is challenging to lower the polarization switching barrier while maintaining the dielectric breakdown strength of the material. Until 2019, Fichtner et al. demonstrated the ferroelectric polarization switching in AlScN with P_r of 110 μC cm^{-2} [99]. Immediately afterward, a large amount of research work

© The authors https://doi.org/10.1007/s40820-024-01441-1

explored the factors affecting the ferroelectricity of AlScN. In order to more objectively evaluate the impact of Sc content on the ferroelectricity of AlScN, the research data from different groups are compiled here for comparison (Fig. 6). As mentioned in Sect. 3.1, Sc doping can reduce the energy barrier between the two polarization states of $Al_{1-x}Sc_xN$, allowing polarization reversal under external voltage. This has been experimentally confirmed. With the increase in Sc content, the E_c of AlScN decreases (Fig. 6d), implying that the switching barrier of AlScN is indeed lowered with the incorporation of Sc. The evolution of E_c in $Al_{1-x}Sc_xN$ with the Sc content (x) satisfies the following relationship: $E_c(x) = -15x + 8.35$ (MV cm^{-1}) ($0 < x < 0.43$) [130]. However, when the Sc content is greater than 30%, the full width at half maximum (FWHM) of the rocking curve for (0002) diffraction peak shows a step increase, indicating that crystallization deterioration is observed (Fig. 6a). The reduction of the switching barrier of AlScN through the incorporation of Sc is generally regarded to relate with the in-plane tensile strain generated by the structural distortion of the wurtzite crystal, which can be confirmed by the decrement of c/a values in Fig. 6b [131]. As the Sc content further increases, $Al_{1-x}Sc_xN$ gradually transforms from the ferroelectric wurtzite phase to the non-ferroelectric rock salt phase, and the P_r value rapidly decays (Fig. 6c). In-plane mechanical stress on AlScN film yielded similar impacts. With the in-plane mechanical stress changes from − 0.8 to + 0.5 GPa, E_c decreases from 5 to 4 MV cm^{-1} [99]. Both Sc doping and tensile stress have a tendency for fivefold coordination in a ScN-like planar hexagonal structure, leading to a sufficient energetic destabilization of the wurtzite structure to allow for ferroelectric switching. In addition, the permittivity of $Al_{1-x}Sc_xN$ slightly increases with the increase in Sc content (Fig. 6e). To obtain better ferroelectric performance, Sc

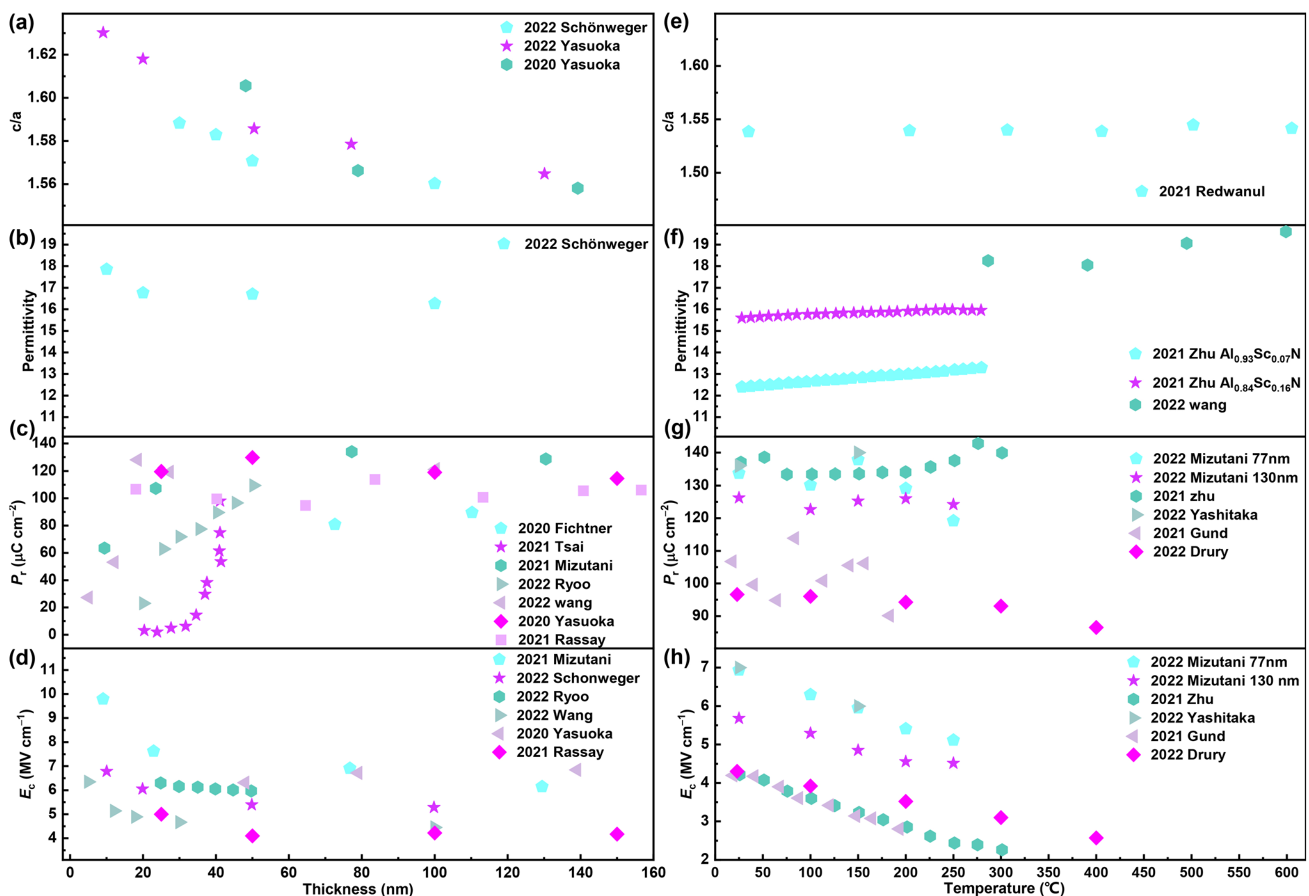

Fig. 7 Material properties of $Al_{1-x}Sc_xN$ as a function of the film thickness. **a** *c/a*, **b** permittivity, **c** *Pr* and **d** *Ec*. The material properties of $Al_{1-x}Sc_xN$ as a function of temperature. **e** *c/a*, **f** permittivity, **g** *Pr* and **h** *Ec*. Data from Ref. [99, 101, 103, 104, 126, 127, 133–139]

content and in-plane stress should be optimized for reducing the E_c and leakage current and maintaining the breakdown strength [100, 132].

The thickness dependence of ferroelectricity of $Al_{1-x}Sc_xN$ films was comprehensively explored. For the case of in-plane tensile strain generated by the substrate, the strain will relax with the increase in film thickness. Correspondingly, the c/a of $Al_{1-x}Sc_xN$ decreases with the increase in film thickness within 50 nm and tends to be stable for film thickness greater than 50 nm (Fig. 7a). The dielectric constant of $Al_{1-x}Sc_xN$ is slightly affected by the film thickness (Fig. 7b). As the film thickness decreases, the measured P_r value of $Al_{1-x}Sc_xN$ decreases. This decay phenomenon of polarization in thinner films is mostly related to the dead layer at interface (Fig. 7c). A good epitaxial quality can endow a high P_r value of 100 μC cm^{-2} at 100 °C for a 9-nm $Al_{1-x}Sc_xN$ films [101]. Following a nucleation dynamics, the scaling of the E_c with thickness in traditional ferroelectric films obeys $E_c \propto d^{-2/3}$, where d is thickness of the ferroelectric films [140]. In $Al_{1-x}Sc_xN$ thin films, as the thickness decreases, the E_c remains relatively stable and begins to increase when the film thickness reaches below 20 nm (Fig. 7d) [141].

Vast reports reveal that $Al_{1-x}Sc_xN$ exhibits stable temperature dependence. The c/a of $Al_{1-x}Sc_xN$ slightly change with temperature (Fig. 7e) [60]. As the temperature increases, the permittivity of $Al_{1-x}Sc_xN$ also changes very little, less than 5% within 600 °C (Fig. 7f). Within 400 °C, the P_r of $Al_{1-x}Sc_xN$ shows good temperature stability (Fig. 7g). In addition, the E_c of $Al_{1-x}Sc_xN$ decreases with the increase in temperature. From room temperature to 300 °C, the E_c of $Al_{1-x}Sc_xN$ decreases by half (Fig. 7h). However, compared with other ferroelectric materials, this E_c value is still too large.

3.3 Polarization Switching in Ferroelectric AlScN

It is important to explore the polarization switching mechanism of ferroelectric AlScN. The regions with uniform spontaneous polarization in ferroelectrics are called domains, and the boundaries between domains with different polarization directions are called domain walls. Generally, according to whether the angle between the spontaneous polarization directions of two adjacent domains is 180°, they are divided into 180° domain walls and non-180° domain walls [143]. Common non-180° domain walls include 90° domain walls, represented by the tetragonal and orthorhombic phases, and 71° and 109° domain walls represented by the rhombohedral phase [144]. The polarization switching process of ferroelectrics includes domain nucleation and growth. Lu et al. used piezoresponse force microscopy (PFM) that combines a pulse testing to reveal the evolution of the domain structure of $Al_{0.72}Sc_{0.28}N$ capacitors over time under different voltages [142]. $Al_{0.72}Sc_{0.28}N$ capacitors have P_r exceeding 150 μC cm^{-2}, and its hysteresis loop has a steep slope (Fig. 8a). With the increase in voltage (from 11.5 to 15.5 V), the switching time of $Al_{0.72}Sc_{0.28}N$ capacitor decreases by three orders of magnitude, which is consistent with the changes in domain structure displayed by PFM over time at different voltages (Fig. 8b, c). Zhang et al. observed the formation of ferroelectric domains in AlN that has some Sc content, through 4D-STEM differential phase contrast mapping [145]. The same characterization method also revealed the distribution of ferroelectric domains in single-crystal AlScN nanowires [146]. Kim et al. confirmed that the domain nucleation growth mechanism of AlScN satisfies the inhomogeneous field model (IFM) [147]. The characteristic switching time limit of AlScN (5.98×10^{-14} s) is more than three orders of magnitude faster than that of HZO (1×10^{-10} s), while its activation field (96 MV cm^{-1}) is one order of magnitude higher than that of HZO (8.94 MV cm^{-1}), accounting for the high E_c of AlScN. Schönweger et al. firstly reported inversion domain boundaries in single crystal of AlScN, which supports the domain reversal theory of gradual domain-wall driven switching process (Fig. 9a) [106].

Polarization switching of AlScN on a macroscopic scale has been observed. The crystal cell orientation of wurtzite semiconductors (GaN, AlN, etc.) can be verified through acid–base etching (H_3PO_4, KOH, etc.) [149]. The surface of N-polar is easy to be etched by acid and alkali, with conical shape remaining on the surface, while the metal-polar surface is almost not etched (except for local defects and reverse domains) [150]. Niklas et al. confirmed the conversion of N-polar to metal-polar after ferroelectric polarization by H_3PO_4 etching method. The corresponding scanning electron microscope (SEM) shows the conical morphology of the N-polar surface after etching and transition from N-polar surface to metal-polar surface after polarization reversal (Fig. 9b).

At the atomic scale, when ferroelectrics undergo polarization switching under the action of an electric field, it is often

© The authors https://doi.org/10.1007/s40820-024-01441-1

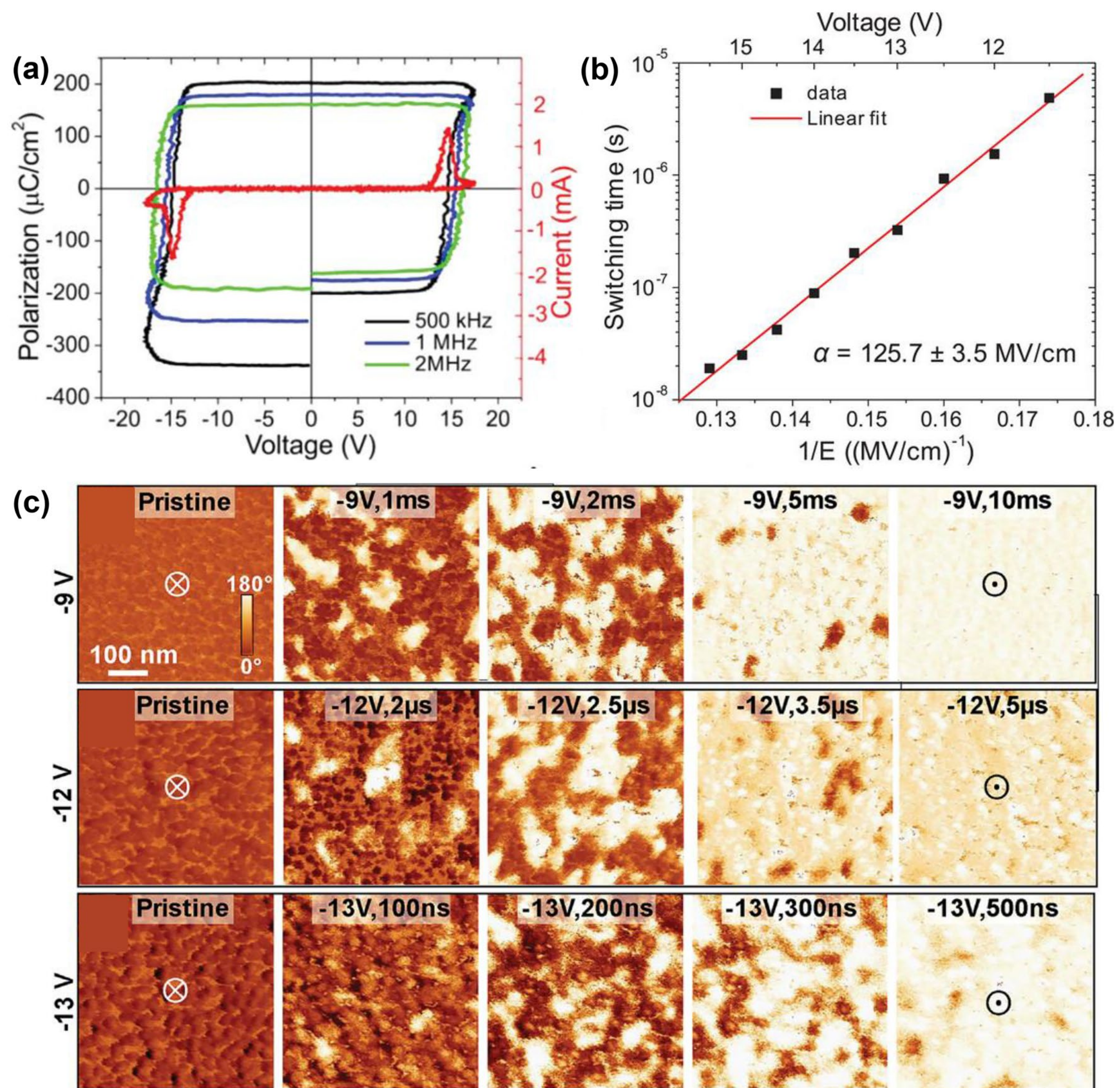

Fig. 8 **a** *P–V* loops of $Al_{0.72}Sc_{0.28}N$ at various frequencies. **b** Switching time as a function of the pulse amplitude. **c** PFM phase images of $Al_{0.72}Sc_{0.28}N$ after exerting voltage pulse with amplitude of −9 V, −12 V and −13 V. Reproduced with permission from Ref. [142]. Copyright 2024 Wiley-VCH GmbH

accompanied by the relative displacement of anions and cations [152]. For example, $BaTiO_3$ is the displacement of Ba^{2+} cations relative to Ti–O octahedron, while in HfO_2-based ferroelectrics it is the displacement of O^{2-} anions relative to metal cations [141]. As we know, the polarity of AlN is derived from the relative separation of Al^{3+} and N^{3-} anions. Combined with the previous experience of traditional ferroelectrics, the polarization switching of AlScN under the action of an electric field is also accompanied by the relative displacement of metal cations and N^{3-} anions.

The transformation of N-polar to metal-polar after ferroelectric polarization is confirmed from the atomic scale by STEM. The green frame line is the initial N-polar surface and the red frame line is the metal-polar surface after inverted polarization (Fig. 10a). The images of high angle

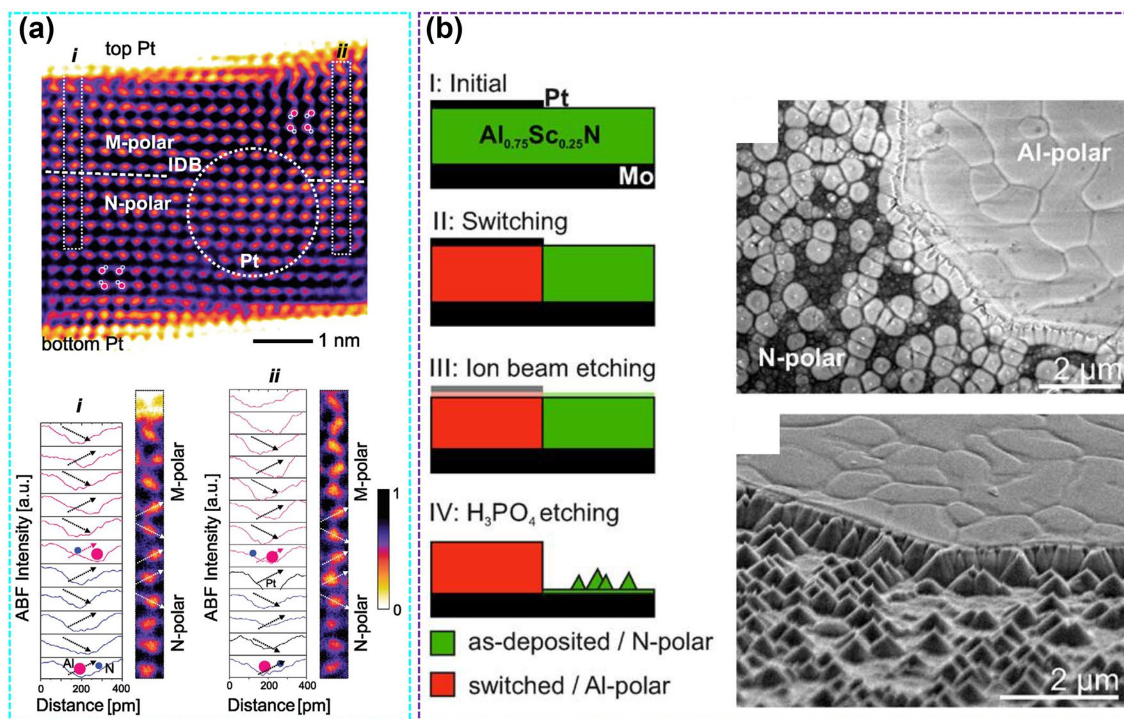

Fig. 9 **a** STEM micrographs of the M- and N-polar domain boundaries of $Al_{0.74}Sc_{0.26}N$. Reproduced with permission from Ref. [106]. Copyright 2023 Wiley-VCH. **b** Schematic diagram of determining local metal or N-polar by H_3PO_4 etching method. Reproduced with permission from Ref. [148]. Copyright 2021 AIP Publishing

annular dark field (HAADF) in the green area show obvious N-polar (Fig. 10b), while the images of HAADF in the red area show that the unit cell polarity is reversed from N-polar to metal-polar (Fig. 10c) [148]. Sebastian et al. successfully observed the atomic-scale polarization switching process of AlN-based ferroelectrics during voltage application through in situ STEM, that is, from the initial (N-polar), intermediate (nonpolar) and final (Al-polar) switching sequence (Fig. 10d) [151]. So, the polarization switching of ferroelectric AlScN is the mutual switching between metal-polar and N-polar under the action of an electric field, and this process is accompanied by the relative displacement of metal (Al^{3+} and Sc^{3+}) cations and N^{3-} anions under the action of an electric field.

The above insights into the macroscale and in situ atomic-scale processes of polarization switching in AlN-based ferroelectric materials provide guidance for future research on other wurtzite-structured ferroelectric materials, and it also provides a strong theoretical support for the future commercial application of AlN-based ferroelectrics.

3.4 Performance Optimization of AlScN Films Grown by Different Deposition Techniques

It is essential to fabricate high-quality AlScN films to meet the application requirements. So far, AlScN thin films can be deposited through the various techniques, including molecular beam epitaxy (MBE), magnetron sputtering (MS), metal–organic chemical vapor deposition (MOCVD) and pulsed laser deposition (PLD). First of all, it is important to understand that both Al and Sc have high oxygen affinity, so AlScN needs to be grown in a high vacuum environment to avoid oxygen defects. Substrates, such as typically Pt (111), Mo (110), Al (110), GaN, AlN, Al_2O_3 and other substrates can provide a hexagonal template for AlScN.

The advantages of MS include relatively low cost, good repeatability, strong adhesion between the film and the substrate, and the ability to deposit films with different element content [153]. MS deposition of AlScN commonly uses Al/Sc alloy targets or employing co-sputtering via two metal

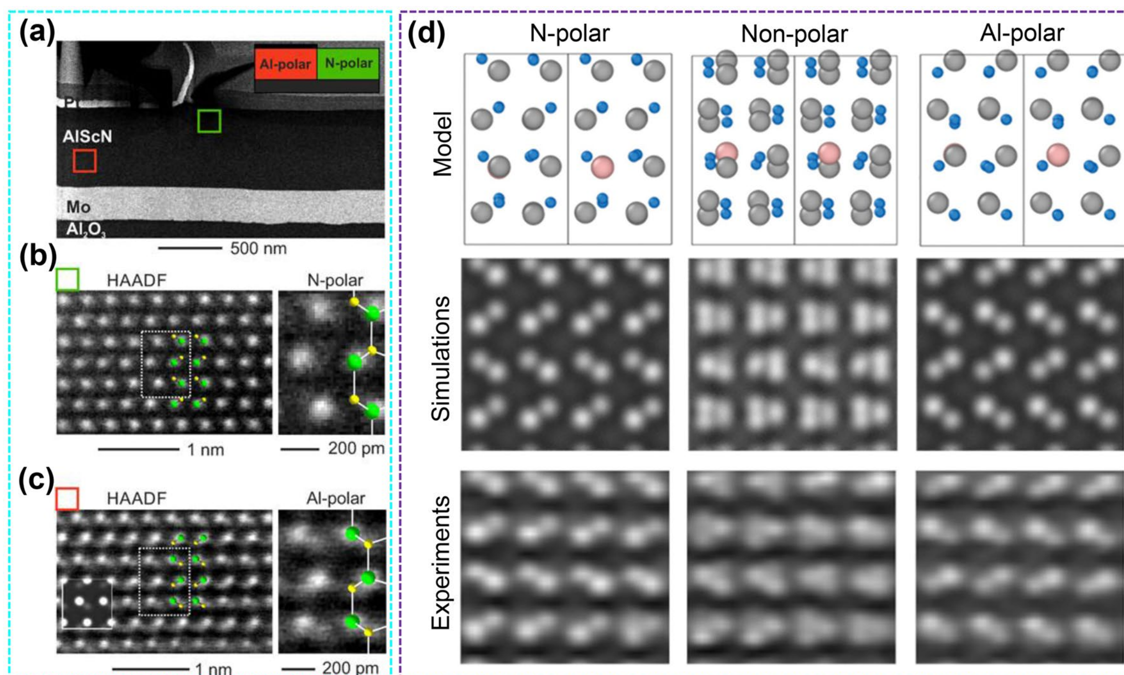

Fig. 10 **a** STEM image of deposited Pt area with polarization switched to metal-polar and unswitched area (N-polar). **b** HAADF micrographs show the atomic structure of N-polar. **c** HAADF micrographs show the atomic structure of metal-polar after polarization reversal in the deposited Pt region. Reproduced with permission from Ref. [148]. Copyright 2021 AIP Publishing. **d** Atomic models, STEM image simulations and experimental images for the N-polar, nonpolar and Al-polar states. Reproduced with permission from Ref. [151]. Copyright 2023 AAAS

targets. The alloy target offers a higher deposition rate, which can ensure uniform composition across the entire wafer and thus is suitable for industrial applications. However, adjusting the scandium content in the alloy target can be challenging, and the complex metallurgical processes involved may result in higher costs. Co-sputtering can tune the Sc concentration by adjusting the power of the single target, which is lower in cost. However, reducing the power of the single target can compromise the uniformity and crystallinity of the film. Parameters such as power, N_2/Ar ratio, background pressure and growth temperature during sputtering affect the sputtering rate, film quality, surface roughness and electrical properties of AlScN. For example, the N_2/Ar ratio governs both the sputtering rate and nitridation reaction, while the sputtering power regulates the sputtering rate and crystallinity. Background pressure impacts the sputtering rate, whereas growth temperature influences the grain size, film surface stress and crystallinity. Chiu et al. studied the effect of sputtering conditions on the crystal quality of AlN thin films [154]. They identified the optimal deposition conditions for AlN as follows: power = 1400 W, N_2/Ar = 80%, background pressure = 0.8 Pa and growth temperature = 400 °C. A few studies have reported the impacts of different deposition conditions on the ferroelectricity of AlScN. For example, increasing the N_2/Ar ratio leads to higher values of both P_r and E_c increase, alongside the decreased film roughness and increase the stress [155]. The AlScN film is deposited at 400 °C exhibits the highest P_r [156]. Ryoo et al. systematically investigated the effects of different magnetron sputtering parameters (power, N_2/Ar ratio, background pressure and growth temperature) on the ferroelectric properties of $Al_{0.7}Sc_{0.3}N$. The exploration of depositional conditions is outlined in Table 1, and will not be further discussed here. The optimum deposition conditions of $Al_{0.7}Sc_{0.3}N$ on TiN were determined as follows: power = 500 W, N_2/Ar = 100%, background pressure = 20 mTorr and growth temperature = 300 °C. Under these deposition conditions, the maximum saturated 2 P_r of 120 μC cm^{-2} for 25-nm films was observed, which was about half of that in 50-nm-thick films (≈ 220 μC cm^{-2}) [135]. The substrates with different thermal expansion coefficients also impact the ferroelectric properties of AlScN films. Due to

Table 1 Effect of MS deposition conditions on the ferroelectric properties of AlScN. Data collected from Ref. [135]

	c (Å)	a (Å)	Lattice volume (Å^3)	Deposition rate (nm min^{-1})	Grain diameter (nm)	Roughness (nm)	Sc/(Sc + Al)	P_r (μC cm^{-2})	E_c (MV cm^{-1})
Power									
300 W	4.981	3.211	133.411	1.02	13.154	0.403	0.304	145.84	5.69
400 W	4.986	3.198	132.453	1.632	12.258	–	0.308	153.33	5.78
500 W	4.988	3.194	132.181	2.28	13.338	0.725	0.306	153.5	5.83
600 W	4.997	3.19	132.076	2.928	14.392	0.733	0.316	134.18	5.94
N_2/Ar									
20%	4.99	3.218	134.248	2.97	12.418	0.593	0.308	113.45	5.62
40%	4.999	3.214	134.133	2.562	–	0.668	–	141.8	5.75
60%	4.997	3.203	133.173	2.28	14.072	0.685	0.297	153.35	5.8
80%	5.005	3.202	133.289	2.25	–	0.802	–	159.35	5.81
100%	5.017	3.192	132.768	2.1	13.832	0.992	0.300	156.2	5.92
Pressure									
5 mTorr	5.001	3.192	132.405	2.04	13.646	0.977	0.296	142.9	6
10 mTorr	5.001	3.186	131.866	1.806	12.29	0.817	0.312	161.6	6.1
15 mTorr	5.031	3.198	133.663	1.548	10.936	0.773	0.298	159.71	6.2
20 mTorr	5.064	3.203	134.995	1.35	9.136	0.717	0.302	177.83	6.37
Temperature									
RT	5.052	3.189	133.501	1.272	10.626	0.898	0.308	161.5	6.34
150°C	5.024	3.185	132.431	1.272	11.2	0.822	0.303	174.7	6.12
300°C	5.015	3.195	133.01	1.29	12	0.392	0.296	201.43	6
400°C	5.012	3.2	133.333	1.26	11.8	0.301	0.297	186.2	5.9

the existence of thermal stress, the lattice parameters of the films are affected. Results demonstrate that the P_r and E_c of the AlScN film decrease with the decrease in the thermal expansion coefficient of the substrate [157]. High Sc content can lead to impurities (rock salt) formation and an increase in defect density, which can affect crystal quality and elevate leakage current. In addition, the MS technique used to deposit AlScN epitaxial films on single-crystal GaN substrates is accompanied by a competition between M-polar and N-polar, especially when AlScN exceeds 30 nm, resulting in the coexistence of multiple domains [127]. Table 2 summarizes the conditions for depositing AlScN with MS and the corresponding ferroelectric properties of AlScN.

The epitaxial growth of AlScN on GaN, AlN, SiC, Al_2O_3 and Mo substrates can be achieved through MBE, MOCVD and PLD techniques. The advantage of MBE is that ultra-thin epitaxial films with high uniformity can be prepared, and multilayer structure with different dopants or components can be realized [166]. At present, the temperature for depositing AlScN by MBE is typically above 500 °C. Wang et al. grew AlScN epitaxial films on GaN substrates by MBE, and confirmed that the optical bandgap of AlScN decreased with the increase in Sc content. The $Sc_{0.20}Al_{0.80}N$ grown by MBE almost matches the GaN lattice, showing a E_c of ~ 4.2 MV cm^{-1} and a P_r of ~ 135 μC cm^{-2}. The polarization retention time of $Sc_{0.20}Al_{0.80}N$ is more than 10^5 s and there is no fatigue behavior with 3×10^5 cycles [109]. In order to meet the requirements of low-power memory and CMOS compatibility, devices need to operate at low voltages, grow on Si substrates at low-temperature. Reducing the film thickness can reduce the operating voltage [167]. Wang et al. have grown 5–100-nm-thick $Al_{0.7}Sc_{0.3}N$ epitaxial film on Mo/Si substrate. With the decrease in film thickness, the E_c increases while the P_r decreases. Specifically, 5 nm thick $Al_{0.7}Sc_{0.3}N$ can achieve P_r of 23 μC cm^{-2} at 2–3.8 V [104]. Growth in a nitrogen-rich environment can ensure the phase purity and crystal quality of wurtzite AlScN, but can lead to increased film roughness [168]. Hardy et al. grew high-quality AlScN films at 390 °C, enabling growth of AlScN at COMS compatible process temperature [169].

© The authors
https://doi.org/10.1007/s40820-024-01441-1

Table 2 MS deposition of AlScN

Substrate	Target	Sc composition	Growth temperature (°C)	Thickness (nm)	FWHM (°)	P_r (μC cm^{-2})	E_c (MV cm^{-1})	References
AlN/Pt	AlSc alloy	0.27–0.43	400	400–1000	–	75–110	2–5	[99]
Pt/TiO_x/SiO_2/Si	Al and Sc	0.1–0.34	400	9–140	2–2.7	3.8–135	–	[126]
Pt/Si	Al and Sc	0.29	350	100	–	80	–	[158]
Pt(111)/Ti/ SiO_2/Si(100)	Al and Sc	0.36	–	20	2.8	30	6.5	[159]
Al_2O_3	Al and Sc	0.16	350	363	–	135	4.2	[103]
Pt/Si	Al and Sc	0.36	350	20	–	25	6.5	[160]
Mo/Si	Al and Sc	0.27	–	400–2000	–	138	4.1	[60]
Mo/AlN/Al_2O_3	Al and Sc	0.25	450	550	2.6	–	–	[148]
Al/$Al_{0.80}Sc_{0.20}N$ /Si	Al and Sc	0.32	150	45	–	115	−4.3/5.3 (10 kHz)	[161]
Pt/SiO_2/Si or Al_2O_3 or MgO	Al and Sc	0.2	400	100		115–127	6.5–7.2	[157]
n-GaN	Al and Sc	0.19–0.28	450	40–300	0.28–0.38	≤ 120	6–12	[127]
Pt/Ta/SiO_2	Al and Sc	0.2–0.45	400	90–200	–	–	–	[162]
Pt(111)/TiO_x/ SiO_2/Si(100)	Al and Sc	0.2	400	12–130	–	~ 135	5–7	[133]
Al	Al and Sc	0.32	375	45	–	120	–	[163]
Pt/TiN	Al and Sc	0.38	RT or 400	15	–	–	–	[164]
Pt/GaN	Al and Sc	0.28	500	100	2.44	~ 175	5	[61]
Pt (111)/Ti/ SiO_2/Si	Al and Sc	0.32–0.36	350	20	2	140	6.5	[62]
TiN	Al and Sc	0.22	400 and RT	50	9.7 at 400 °C, 15.2 at RT	113 at 400 °C, 70 at RT	8.1 at 400 °C, 6.5 at RT	[130]
Pt/TiO_x/SiO_2/Si	Al and Sc	0.2	400	9–130	–	> 100	6–10	[101]
Pt/TiO_x/SiO_2/Si	Al and Sc	0.22	25–500	120–190	–	10–129	6–8	[165]
Pt/GaN	Al and Sc	0.28	450	10–100	0.1–2	–	5.5–6.5	[107]
Pt	$Al_{0.7}Sc_{0.3}$ alloy	0.3	400	225	2.694	100	4.3	[102]

Table 3 Epitaxial deposition of AlScN

Method	Substrate	Sc composition	Growth temperature (°C)	Thickness (nm)	FWHM (°)	P_r (μC cm^{-2})	E_c (MV cm^{-1})	References
MBE	*n*-GaN	0.17–0.25	600	100	0.03–0.05	–	–	[129]
	Si <111>	0.03–0.26	–	400–800	1.1	–	–	[170]
	Si-doped-GaN	0.2	–	200	–	70–80	4.6	[171]
	n-GaN	0.18–0.4	600–750	25–30	0.09–0.12	–	–	[172]
	Si	0.12	–	400	1.2	–	–	[173]
	AlN	0.06–0.32	700/390	200	–	–	–	[169]
	GaN/AlN	0–0.34	400–900	50–100	–	–	–	[174]
	Si-doped-GaN	0.14–0.36	–	100	–	135	3.4–5.7	[59]
	Si-doped-GaN	0.21	–	–	0.31	90	4.9	[175]
MOCVD	GaN/Al_2O_3	0.05–0.17	1000–1200	6.5–16.9	–	–	–	[176]
	GaN/Al_2O_3	0.2–0.3	1000	10–100	0.07	–	–	[177]
PLD	Mo/Si	0.3	–	100	–	140	5	[178]

It is noteworthy that the ferroelectric properties of AlScN grown by MBE are comparable to those of AlScN grown by MS. Table 3 summarizes the epitaxial deposition of AlScN and its ferroelectric properties under corresponding deposition conditions.

MOCVD can control the composition and doping level of compounds by quickly switching gas source. It facilitates the growth of the single-crystal film over large area with high uniformity and repeatability, achieving a relatively high growth rate (micron h^{-1}), so it stands as the preferred technology for the manufacturing nitride semiconductors (AlN, GaN) [179]. However, a significant challenge of growing AlScN by MOCVD lies in the lack of Sc precursors capable of providing sufficient vapor pressure. In 2019, Stefano et al. successfully deposited $Al_{1-x}Sc_xN$ ($x=0.05$–0.17) epitaxial film on GaN substrate at 1000–1200 °C using tris-cyclopentadienyl-scandium as the precursor of Sc for the first time [177]. SiN_X-passivated AlScN/GaN heterostructures are used to fabricate a high-electron mobility transistor based on AlScN, demonstrating a transconductance of nearly 500 mS mm^{-1} [176]. Moreover, the purity of the Sc precursor source affects the leakage current [180]. However, there is currently no report on the ferroelectricity of AlScN grown by MOCVD. Recently, Liu et al. deposited 100-nm-thick $Al_{0.7}Sc_{0.3}N$ thin film on Mo substrate by PLD, with P_r of 140 μC cm^{-2} and E_c of 5 MV cm^{-1} [181]. The advantage of PLD is its capability to obtain multi-component films with desired stoichiometry, but it is not easy to produce large-area films [178].

In addition, the preparation of 10 nm AlN with a P_r of 3 μC cm^{-2} using atomic layer deposition (ALD) technology has been reported [182], and with deposition carried out at 300 °C [183]. Deposition of AlScN by ALD hold promise, as it is compatible with existing CMOS processes and has the potential to be used for the fabrication of complex structures such as 3D NAND and gate-all-around FET. However, it is necessary to prepare a Sc precursor source with low evaporation temperature, and overcome problems such as oxygen defects caused by the poor vacuum level (~ 5 Pa) of ALD. Each of the aforementioned deposition techniques has its own advantages. However, it is no doubt that MS is the most favorable technology for depositing AlScN thin films from the perspectives of cost, reproducibility, adhesion of films to substrates, flexibility of deposition target materials and potential for wafer-level manufacturing.

4 AlScN FeM and Its Application in IMC

Research interest in ferroelectric AlScN has been aroused due to its potential in low-power memory and neuromorphic computing. This chapter aims to present an overview of AlScN-based FeM from the perspective of commercial memory requirements, and to explore its application in IMC.

4.1 Potential Application of AlScN in FeRAM

The current commercial DRAM mainly adopts the memory cell structure of one transistor plus one capacitor (1T1C). The capacitor is like a "cistern" responsible for storing the charge as information, and the transistor works as a "faucet" to avoid the loss of charge over time [92, 184, 185]. FeRAM shares similar structure with DRAM, except that the dielectric layer is replaced by ferroelectric material with the remanent polarization charge encoded as information [186]. Since FeRAM adopts metal–ferroelectric–metal (MFM) structure in which the ferroelectric polarization is nonvolatile, data retention is extended and the refresh operation to prevent data loss can be omitted, therefore reducing power consumption. Besides, the nanosecond or even sub-nanosecond polarization switching speed endows fast operation in FeRAM. Despite these advantages of FeRAM, several issues remain to be resolved. With the density scaling of FeRAM, it would be preferred to use ferroelectric materials of high P_r and low dielectric constant to increase the sensing margin. Besides, the reading operation of FeRAM is destructive as DRAM [187]. The charge stored in the capacitor is selectively turned on by the transistor and released to the sense amplifier to determine the storage state. After each reading, reprogramming is indispensable to restore information; therefore, the capacitor should have sufficiently high endurance and moderate E_c is desirable. Because of pulse-width dependence of the switching voltage, the trade-off between operating speed and voltage necessitates an electric field twice that of the coercive field for operation. On one hand, a large E_c permits a big memory window and excellent retention behavior. On the other hand, given that operation voltage scales with the

© The authors
https://doi.org/10.1007/s40820-024-01441-1

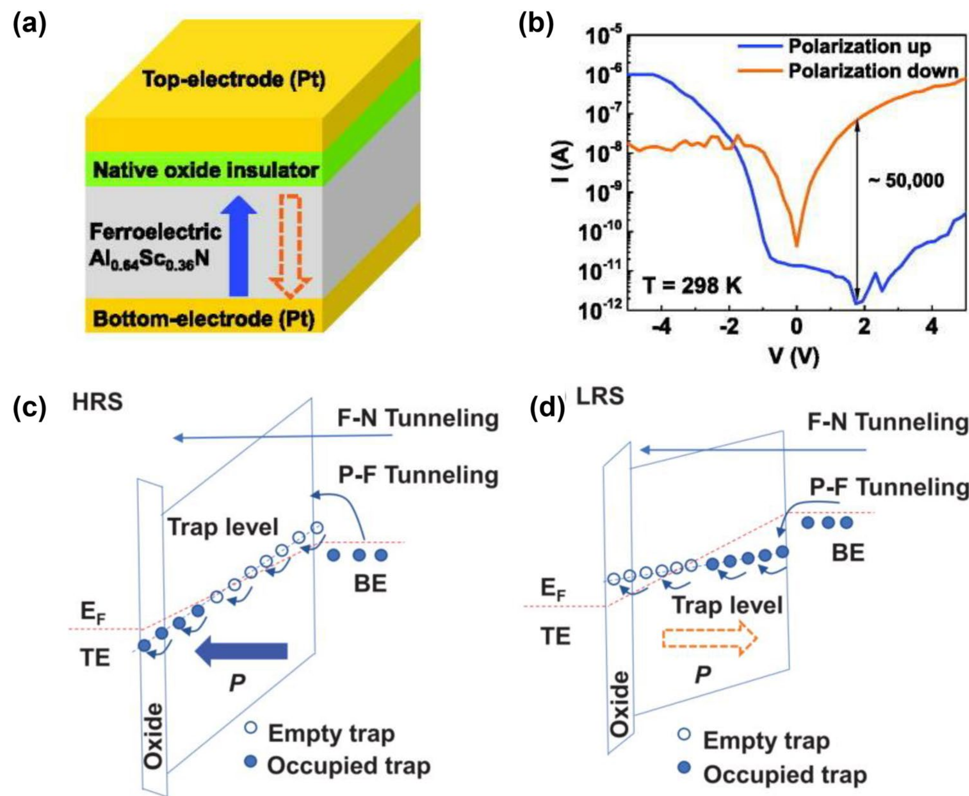

Fig. 11 **a** $Al_{0.64}Sc_{0.36}N$-based FeD. **b** Semi-log *I–V* curve characteristics of the FeD. Electronic band diagrams of **c** HRS and **d** LRS in the FeD. Reproduced with permission from Ref. [160]. Copyright 2021 AIP Publishing

coercive field E_c and the thickness of ferroelectric film thickness, the E_c of thin AlScN films should be reduced for compatibility with CMOS logic [187]. The wurtzite-structured ferroelectrics with high P_r and low ε seem to be promising for FeRAM only if moderate E_c can be achieved in thin films through optimizing doping concentration and strain level [188].

Despite FeRAM based on wurtzite ferroelectrics has not been reported, MFM capacitors with ferroelectric AlScN are under intensive investigations. Wang et al. designed $Al/Al_{0.68}Sc_{0.32}N/Al$ ferroelectric capacitor with P_r of 115 μC cm^{-2}, which can achieve switching operation within 200 ns, and has no obvious fatigue behavior after 8.7×10^3 cycles [161]. In the process of reducing the thickness of AlScN, Schönweger et al. achieved switching operation of sub-5 nm AlScN at 1 V voltage. Liu et al. unveiled that the electron emission and hopping assisted by N vacancies in the $Al_{0.7}Sc_{0.3}N$ MFM capacitor dominate the leakage current in $Pt/Al_{0.7}Sc_{0.3}N/Mo$ capacitor [178].

4.2 AlScN-Based FeD and FTJ

Although FeDs share similar MFM structure with FeRAM, the nondestructive read operation of FeDs is performed by sensing the current across the heterostructure. Taking the interfacial energy band into account, the barrier height/width modulation at the ferroelectric–electrode interface through polarization reversal was proposed for resistive switching mechanism, usually accompanied by diode-like rectifying characteristics. The polarization-dominated mechanism requires ferroelectric layer with high P_r. Liu et al. fabricated $Pt/insulator/Al_{0.64}Sc_{0.36}N/Pt$ FeD with memristor behavior, the current on/off ratio is 5×10^4 (Fig. 11a, b) [160]. The leakage currents of HRS and LRS are trap-assisted conduction. The ferroelectric polarization charges modulate the band diagram, with a lower barrier height for polarization directed to electrode interface than that for polarization anti-orientated to electrode interface. For the so-called "LRS," injected electrons jump from occupied traps to empty traps,

resulting in high current. Conversely, the electron jumping rate significantly decreases (Fig. 11c, d). Asymmetric structures are usually designed at both ends of FeD to improve the switching ratio and rectification, such as metal–ferroelectric–insulator–metal (MFIM), MFS, MFIS, etc. Large rectifying ratio combined with high nonlinearity can eliminate the need for an access transistor or ovonic threshold switches in array integration. Of course, the depolarization field in the MFIM structure cannot be ignored, which requires a ferroelectric material with a suitably large E_c to offset the depolarization field. Wang et al. further increased the ON/OFF ratio to 10^5 by introducing an oxide layer at the interface between the electrode and AlScN. Since the thickness of ferroelectric layer in FDs generally ranges from tens to hundreds of nanometers, the high switching voltages hinder integration with advanced CMOS nodes and the readout currents limit their miniaturization. Moreover, some experimental results have shown that the resistive switching behavior in FDs could be attributed to filament forming/rupture induced by atomic–ionic transport, which are polytropic in nature, thus suffering from small ON/OFF ratio, undesirable variations, poor retention and large cycle-to-cycle/device-to-device randomness. In some cases, both polarization-dominated mechanism and filament-dominated mechanism are known to co-dominate the resistive switching.

As the thickness of the ferroelectric layer is reduced to a few nanometers, quantum mechanical tunneling through ferroelectrics becomes possible, and the electrical conductivity is greatly enhanced for quantum mechanical tunneling through ferroelectrics and the operating voltage is decreased. These devices with a ferroelectric tunnel barrier sandwiched between two electrodes are called FTJs [189]. The height of the tunneling barrier of FTJ is determined by the state of polarization, so the domain configurations can control the tunneling conductance. Generally, ferroelectric materials with high P_r can deplete the charge at the interface of the FTJ electrode, which increases the width of the tunneling barrier and suppresses the off-state current, giving a large ON/OFF ratio [190]. Of course, by artificially designing asymmetric structures (for example, designing MFS and MFIS) to control the band offset of the tunneling barrier, this can lead to inconsistent shielding lengths at the electrode interfaces on both ends of the device, which can also increase the switching ON/OFF ratio. However, the depolarization field of the above asymmetric structures tends to be large, which requires the ferroelectric layer to have a high E_c to shield the depolarization field. Considering the requirements of the ferroelectric layers in FTJs, AlScN with large P_r and high E_c has great potential for FTJ-based products.

4.3 AlScN-Based FeFETs

In pervasive metal–oxide–semiconductor field effect transistor (MOSFET), the gate voltage applied across the oxide insulator would accumulate or deplete carriers in semiconductor channel, realizing the essential transistor functions of switching and gain, and remaining the backbone of modern electronics. With ferroelectrics as gate insulator, FeFETs yield impressive advances. The polarization charge of traditional ferroelectrics is one or two orders higher than that of oxide dielectrics, inducing more effective modulation of channel conductance in nonvolatile manner. In addition, the continuous and reversible conductance states of FeFETs can be achieved by gradually changing the arrangement of ferroelectric domains. The multiple storage capacity is suitable for high-density data storage and neuromorphic computing. Remarkably, the two-terminal ferroelectric devices have intrinsic drawback for a single shared reading and writing path. FeFETs effectively alleviate this issue by the separation of reading (drain) and writing (gate) terminals.

The most significant performance merits of FeFETs device are ON/OFF ratio, memory window (MW), retention and endurance. The AlScN films with high P_r of ~ 100 μC cm^{-2} support larger carrier density modulation of approximately 10^{14} cm^{-2} than SiO_2 gate dielectric of only about 10^{13} cm^{-2}, achieving high ON/OFF ratio of 10^6 (Fig. 12a). It should be noted that depolarization field (E_{DEP}) can also be increased if P_r is too high, resulting in poor retention. The high E_c of AlScN makes E_{DEP}/E_c low enough, and thus good retention can be obtained (Fig. 12b). Both MW and operating voltage are proportional to E_c and thickness of ferroelectric films. Large MW facilitated by high E_c is essential to correctly distinguish the stored states. However, the high E_c causes high driving power value and a typical endurance of < 10^5 cycles. Based on the above analysis, to achieve better comprehensive performance, the E_c of AlScN film should be modified by changing the Sc concentration, strain engineering and/or superlattice/multilayer construction. It is worth mentioning that the low permittivity of AlScN is

© The authors
https://doi.org/10.1007/s40820-024-01441-1

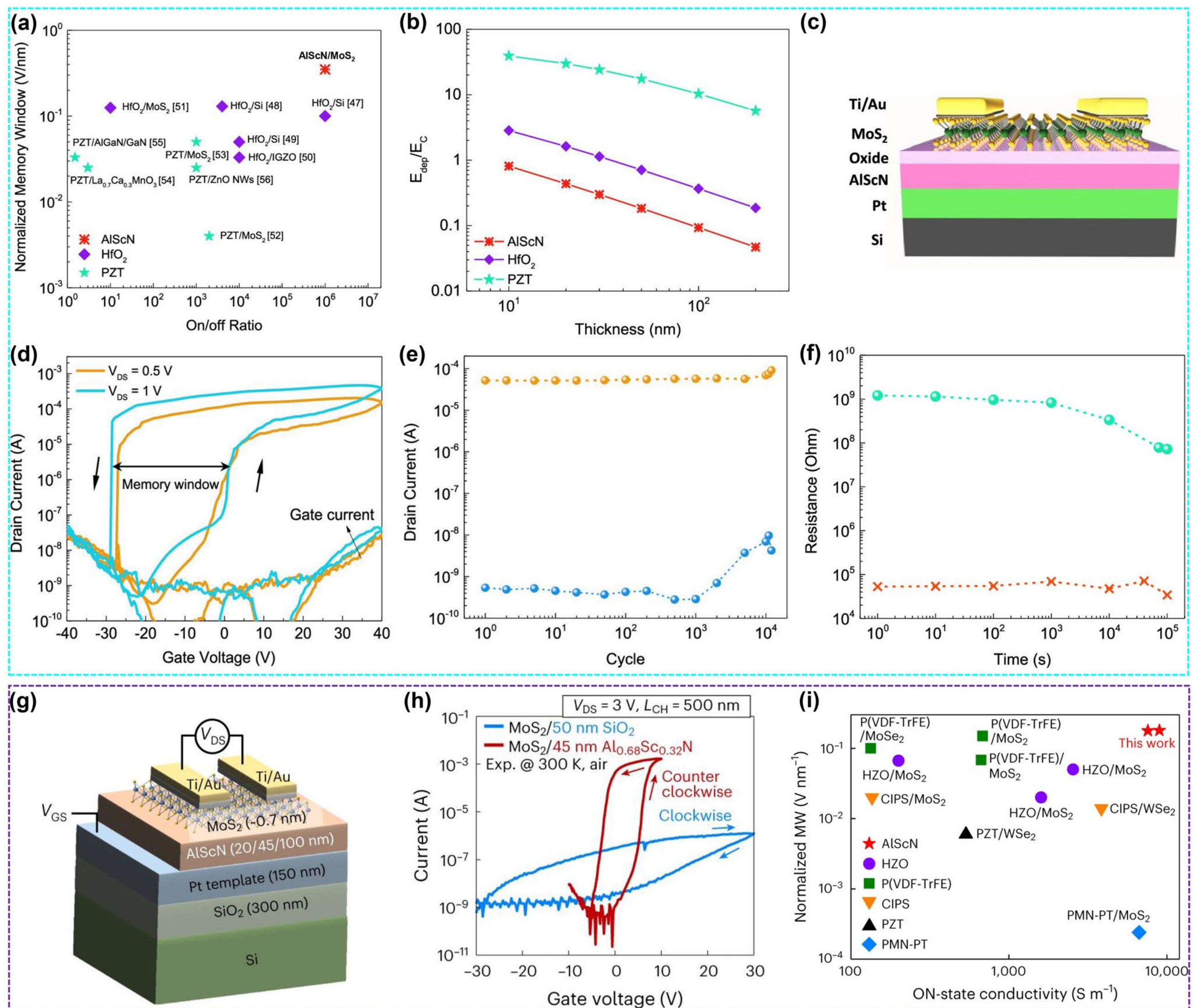

Fig. 12 **a** ON/OFF ratio and normalized storage window of FeFETs (HZO, PZT and AlScN). **b** Simulated values of the ratio of E_{DEP}/E_c for HZO, PZT and AlScN FeFETs. **c** Schematic of AlScN/MoS_2 based FeFETs. **d** *I–V* transfer curve. **e** Endurance and **f** retention of AlScN/MoS_2-based FeFETs. Reproduced with permission from Ref. [158]. Copyright 2021 American Chemical Society. **g** Schematic diagram of AlScN/MoS_2 based FeFETs. **h** *I–V* transfer curve. **i** Comparison of normalized MW and on-state conductivity of FeFETs with different ferroelectric materials and MoS_2 as channel. Reproduced with permission from Ref. [191]. Copyright 2023 Springer Nature

favorable to reduce the electric field in the interfacial layer and improve endurance cycling in MFIS-structured FeFETs.

During the preparation process of FeFETs, there may be defects in the ferroelectric–semiconductor interface, resulting in interface reaction or diffusion, which weakens the quality of ferroelectric layer, and affects the modulation efficiency of FeFETs. Therefore, the ferroelectric–semiconductor interface quality is the key factor determining the performance of FeFETs. As mentioned in Sect. 3.4, most reported $Al_{1-x}Sc_xN$ films have been on highly oriented fcc or bcc metals or TiN, which provide a hexagonal template for growing [001]-direction wurtzite ferroelectrics. There are various wide-bandgap semiconductors such as GaN and SiC that are some degree of lattice matching with $Al_{1-x}Sc_xN$ films, but their integration efforts are mainly focused on high-frequency and high-electron mobility devices. 2D materials provide a solution due to free from dangling bonds, low short-channel effects and ability to be transferred

onto different substrates. Liu et al. demonstrated high-performance FeFET with AlScN as dielectric and 2D MoS_2 as channel (Fig. 12c–f), exhibiting a record normalized memory window (30–40 V) and ON/OFF ratio (10^6), simultaneously with good retention (10^5 s), cycling endurance (> 10^4) and CMOS BEOL compatible processing temperatures (approximately 350 °C) [158]. In this work, MoS_2 flake was mechanically exfoliated from its bulk crystal, a poor option in terms of large-scale applications. Kim et al. adopted CVD and MOCVD methods to prepare large-area MoS_2 films with accurate thickness control (Fig. 12g–i) [191]. A large array of high-performance and scalable FeFETs was demonstrated. Impressively, thanks to the high P_r value of AlScN, the FeFETs hold a large MW of ~ 8 V and an ON/OFF ratio greater than 10^6. The FeFETs display stable retention up to 10 years by extension, and endurance greater than 10^4 cycles. Through voltage-tunable partial switching of ferroelectric domains, 4-bit pulse-programmable memory function and 7-bit operation as artificial synapses are explored. All these merits of MoS_2/AlScN FeFET arrays pave the way toward the ferroelectric memory with silicon CMOS logic.

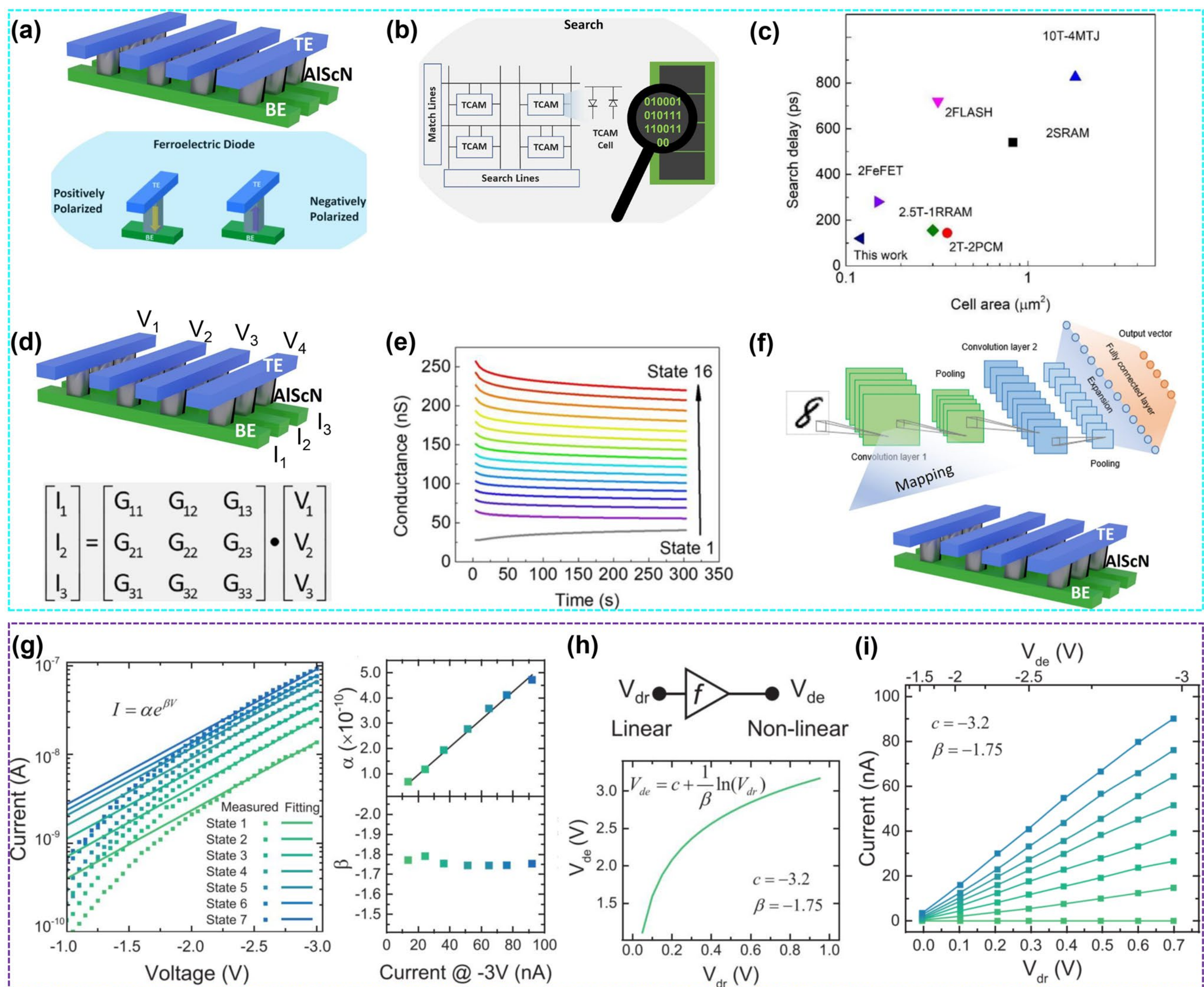

Fig. 13 **a** and **b** Two-FeD TCAM cell for search operation. **c** Benchmark comparison chart of lateral footprint of various TCAM cells vs. search delay. **d** AlScN FD crossbar array implementation of VMM. **e** Retention properties of 16 conductance states. **f** Topology diagram of convolutional neural network. Reproduced with permission from Ref. [163]. Copyright 2022 American Chemical Society. **g** Fitting of the *I–V* curves. **h** and **i** Schematic of a logarithmic driver which maps linear V_{dr} to nonlinear V_{de} for AlScN memristors. Reproduced with permission from Ref. [135]. Copyright 2022 Wiley-VCH

© The authors https://doi.org/10.1007/s40820-024-01441-1

The unavoidable depolarization field in FETs, the low E_c of conventional ferroelectrics and the unsatisfactory ON/OFF ratio hinder the commercial application of FeFETs [192]. Fortunately, ferroelectric AlScN has large E_c to shield the depolarization field and large P_r to modulate the channel conductance withe large ON/OFF ratio, and meets the requirements of CMOS compatibility. Meanwhile, compared with other ferroelectric materials, AlScN has lower permittivity, which increases the voltage loading in the ferroelectric layer. The fatigue characteristics of AlScN FeFETs are already comparable to flash memory, and the read and write speeds are faster than flash memory. Note that flash memory has extremely high integration density and reliability, from the potential commercial view, 3D integration of AlScN FeM needs to be explored.

4.4 AlScN-Based FeM for IMC

As mentioned in Sect. 1, IMC is a solution to solve the memory wall problem [193]. The memory and processor in a von Neumann computer system are separated. The overhead of frequent processor access to memory forms a memory wall [194]. The basic idea of IMC is to improve the computing power of memory through circuit innovation, thereby reducing the frequency of processor access to memory [195]. AI computing requires several basic operations, such as on-chip storage, on-chip parallel search and on-chip VMM, which poses challenges to the reconfigurability and operational flexibility of IMC architectures. On-chip storage is a basic function of all NVM. On-chip parallel search operations require multiple devices to work together and these devices can store states. For example, the operation of ternary content addressable memory (TCAM) requires 16 transistors in CMOS circuits. However, the operation of TCAM based on RRAM also requires 2T2R to complete. Recently, Liu et al. demonstrated that TCAM operation using two AlScN-FeD with opposite polarity as the basic unit (0.12 μm^2/cell) can support three states: "match," "mismatch" and "don't care," with search latency within 100 ps (Fig. 13a–c).

On-chip VMM requires multiple states (such as conductance states) of devices, which is the foundation for neuromorphic computing. Liu et al. developed an AlScN-based FeD crossbar array for IMC, and realized different conductance states by adjusting the polarization states of AlScN-based FeD. This allows the VMM of the input voltage of a word line with the conductance matrix to read the accumulated current on the FeD bit line (Fig. 13d). The FeD unit can be modulated into 16 different conductance states with excellent retention characteristics (Fig. 13e). The conductance is normalized as a weight and stored in the FeD array for VMM. The accuracy of digital recognition (95.5%) for FeD in situ training is only 2% lower than that of software simulation. (Fig. 13f) [163]. For crossbar arrays with good linearity, matrix operations can be directly performed, while nonlinear FeMs require additional fitting of the nonlinear output signal with the linear input pulse signal to obtain linear conductance. Wang et al. designed an ultrathin ScAlN (5 nm)/GaN heterojunction memristor with good retention (> 10^5 s) and cycling endurance (> 10^4), and can be programmed to eight stable conduction states (Fig. 13g). The *I–V* characteristics are fitted using an exponential function, and constant β and linear α values are observed at the conductance level. A mapping function is used to scale the nonlinear device voltage (V_{de}) to a linear drive voltage (V_{dr}). The mapping results demonstrate the realization of linear conductance (Fig. 13h, i). The ScAlN ferroelectric memristor has achieved convolutional processing operations such as main extraction, edge extraction and sharpen, and the accuracy of digital recognition has reached 92.9% [196]. It should be noted here that this memristor was grown on GaN/sapphire substrate, but the n-GaN layer can be replaced with other metals such as Al or Mo, which can be prepared on Si through CMOS compatible processes. Therefore, the memristor and peripheral circuits can be manufactured using BEOL processes. In the latest report of this group, the GaN/ScAlN/Mo/Sc_2O_3/Si heterostructure has been used to simulate the spike-time-dependent plasticity of biological synapses, demonstrating the prospects of ScAlN-based heterostructures for integration with CMOS processes and neuromorphic computing [197].

It is important to emphasize that accurate weights and weight updating are essential for neuromorphic device that is capable of multi-bit operations. When manufacturing ferroelectric-based neuromorphic devices, it is necessary to understand the relationship between conductance and domain states. Thus, the domain dynamics play an important role for realizing these synaptic characteristics of weight updating.

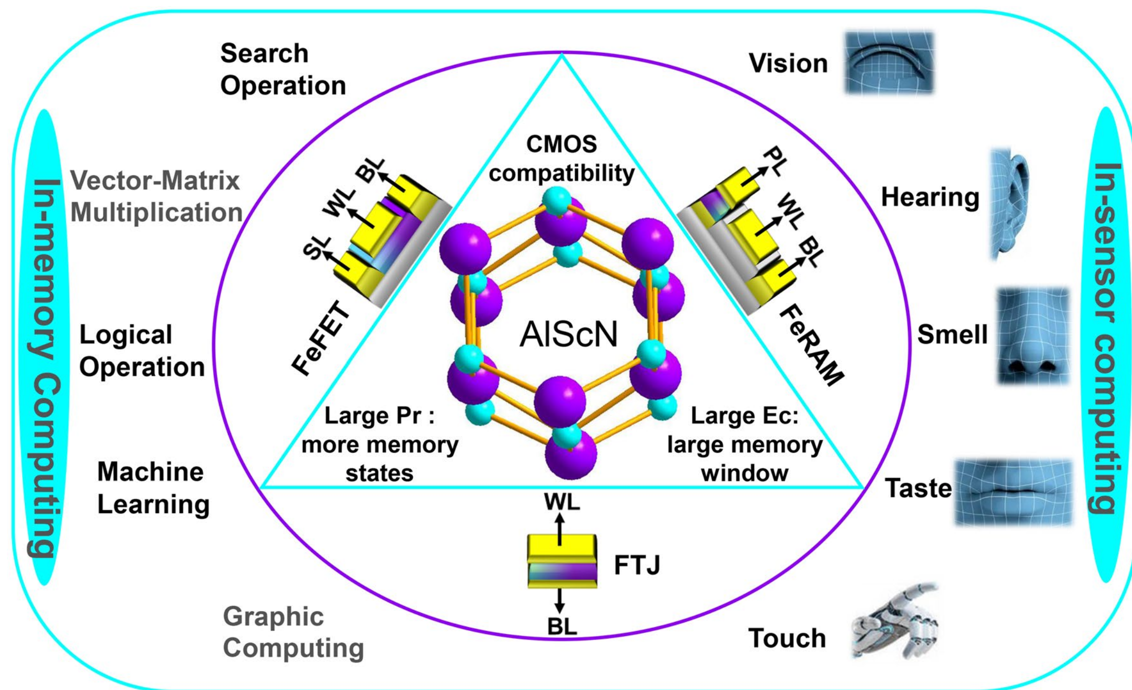

Fig. 14 Advantages of ferroelectric AlScN in NVM and its future application in the field of IMC and in-sensor computing

5 Conclusions and Outlook

Ferroelectric AlScN has advantages such as CMOS back-end of line compatibility, sustainable miniaturization, intrinsic and stable-phase ferroelectricity, which has spurred researchers to extensively explore its physical properties. This review provides a comprehensive summary of AlScN-based ferroelectrics, covering aspects such as the ferroelectric mechanism and domain dynamics, FeMs and their IMC applications. Despite these advancements, the properties of AlScN still require further refinement and development to realize their full potential in future commercial applications.

5.1 The Challenges at the Material Level

The doping of the group III elements can induce stress and reduce the free energy barrier in III-nitrides, leading to polarization reversal of III-nitrides before hard breakdown and accompanied by huge P_r. It is imperative to systematically analyze the influence of factors such as vacancies, temperature, strain, doping concentration, impurities, uneven domains and surface adsorption on ferroelectric properties of AlScN. Currently, in situ PFM combined with pulse testing has confirmed the domain inversion dynamics in AlScN, and the presence of AlScN ferroelectric domain walls has been confirmed with STEM and other methods. However, further investigation using high-precision in situ X-ray diffraction (XRD) and in situ STEM characterization methods is necessary to unravel the origin of AlScN's ferroelectricity and the temperature dependence of ferroelectric properties.

5.2 Demand for AlScN in Commercial Memory

Based on the actual demand of FeM mentioned in Sect. 4, huge E_c is a double-edged sword. The MW of FeFETs is mainly determined by the coercive voltage (V_c) of the ferroelectric layer, proportional to the thickness of the ferroelectric film and the E_c. The miniaturization of devices necessitates a reduction in the gate thickness. Therefore, in order to maintain the required MW, the ferroelectric

© The authors https://doi.org/10.1007/s40820-024-01441-1

gate material in FeFETs devices needs to possess large E_c. Moreover, the incomplete shielding by semiconductor channels in FeFETs introduces large depolarization field, resulting in poor data retention time. High E_c is beneficial for improving the retention characteristics of the device. However, the extremely large E_c requires higher operating voltages and limits the endurance ability of FeRAM. The cycling at high voltages can lead to performance degradation. Consequently, moderate E_c is deemed optimal for achieving balanced performance in ferroelectric applications. The huge E_c of AlScN can be reduced by adjusting the concentration of cations such as the incorporated Ga, B and Sc. Changing the substrate or employing rapid annealing to increase in-plane tensile stress can also decrease E_c [198]. Additionally, the adoption of ultra-thin film is necessary to lower the required voltage level. Should the operating voltage of AlScN be tailored to be compatible with the silicon process, it would unlock boundless potential of AlScN in advanced electronics manufacturing.

The remanent polarization P_r is another critical parameter of ferroelectric materials. While large P_r offers advantages, it also poses challenges. The substantial P_r exhibited by AlScN expands the range of remanent polarization options and enables the generation of strong local electric fields for effective electrostatic doping [12, 26]. For instance, adjusting the amplitude of the applied voltage can yield numerous inner hysteresis loops with varying P_r values. However, in FeFETs, large P_r can result in significant depolarization field. Therefore, in FeFETs applications, a suitable P_r is preferred to balance performance and stability.

When the applied electric field approaches close to E_c, AlScN experiences significant leakage current, resulting in poor cyclic durability. This issue is usually attributed to nitrogen defects, dislocations and uneven domains. A high vacuum deposition system is required to grow thin films in an environment with high nitrogen content to inhibit the formation of nitrogen vacancies. Additionally, fit substrates which can not only provide epitaxial templates to suppress dislocations and uneven domains but also induce appropriate strain to flatten polarization energy profile are indispensable. Furthermore, it is also important to systematically study wake-up effect, imprinting effect, fatigue failure mechanism and cyclic durability mechanism that need to be addressed for the storage application of wurtzite ferroelectric thin films.

In order to meet the demand for AlScN in commercial chips, it is imperative to focus on cost reduction while maintaining the quality of AlScN wafers. Additionally, meeting the requirements of the deep hole filling process is essential. As discussed in Sect. 3.4, the ALD process of AlScN can be employed for deep hole filling of intricate structures, but the defects such as lattice oxygen caused by poor vacuum condition in ALD remain significant concerns. Furthermore, leveraging the performance advantages of wurtzite ferroelectric materials opens avenues for designing novel memory structures and chip architectures.

5.3 Demand for FeM Chips for IMC

In performing VMM computation, the uniformity across devices and cycles is paramount. This underscores the critical need for devices that exhibit consistent performance and high durability, necessitating a deep understanding of the intricate connections between polarization states, domain dynamics, and resistance within the device. At present, AlScN-based devices remain relatively rudimentary, often existing in simplistic configurations as single units. To advance toward IMC, there is a pressing demand for high-quality, large-scale fabrication of device arrays. For FTJ and FeD, achieving sufficiently compact unit sizes and enabling multilevel states are crucial for optimal performance. In the case of FeFETs, adapting NAND-like structures presents a viable approach to enhance storage density.

In summary, ferroelectric AlScN demonstrates excellent ferroelectricity and has broad application prospects in the field of ferroelectric NVM. While addressing the aforementioned challenges, it is crucial to focus on adjusting the electrical properties of ferroelectric AlScN and exploring an integrated process compatible with both front-end and back-end technologies. Of course, it is essential to expand the application of AlScN in IMC (such as search operation, vector–matrix multiplication, logical operation, machine learning and graphic computing) and in-sensor computing (such as artificial vision, hearing, touch, smell and taste sensors) (Fig. 14). Despite the potential time required for commercialization, it is anticipated that the outstanding performance of AlScN will lead to widespread applications once its films and devices achieve critical mass.

Acknowledgements Thank fundings of National Natural Science Foundation of China (No. T2222025, 62174053 and 61804055),

National Key Research and Development program of China (No. 2021YFA1200700), Shanghai Science and Technology Innovation Action Plan (No. 21JC1402000 and 21520714100) and the Fundamental Research Funds for the Central Universities.

Declarations

Conflict of interest The authors declare no interest conflict. They have no known competing financial interests or personal relationships that could have appeared to influence the work reported in this paper.

Open Access This article is licensed under a Creative Commons Attribution 4.0 International License, which permits use, sharing, adaptation, distribution and reproduction in any medium or format, as long as you give appropriate credit to the original author(s) and the source, provide a link to the Creative Commons licence, and indicate if changes were made. The images or other third party material in this article are included in the article's Creative Commons licence, unless indicated otherwise in a credit line to the material. If material is not included in the article's Creative Commons licence and your intended use is not permitted by statutory regulation or exceeds the permitted use, you will need to obtain permission directly from the copyright holder. To view a copy of this licence, visit http://creativecommons.org/licenses/by/4.0/.

References

1. M. Hilbert, P. López, The world's technological capacity to store, communicate, and compute information. Science **332**, 60–65 (2011). https://doi.org/10.1126/science.1200970
2. R. Huo, S. Zeng, Z. Wang, J. Shang, W. Chen et al., A comprehensive survey on blockchain in industrial Internet of Things: motivations, research progresses, and future challenges. IEEE Commun. Surv. Tutor. **24**, 88–122 (2022). https://doi.org/10.1109/COMST.2022.3141490
3. M. Mohammadi, A. Al-Fuqaha, S. Sorour, M. Guizani, Deep learning for IoT big data and streaming analytics: a survey. IEEE Commun. Surv. Tutor. **20**, 2923–2960 (2018). https://doi.org/10.1109/COMST.2018.2844341
4. S. Gao, X. Yi, J. Shang, G. Liu, R.-W. Li, Organic and hybrid resistive switching materials and devices. Chem. Soc. Rev. **48**, 1531–1565 (2019). https://doi.org/10.1039/c8cs00614h
5. C. Seife, Big data: the revolution is digitized. Nature **518**, 480–481 (2015). https://doi.org/10.1038/518480a
6. M.S. Gordon, T.L. Windus, Editorial: modern architectures and their impact on electronic structure theory. Chem. Rev. **120**, 9015–9020 (2020). https://doi.org/10.1021/acs.chemrev.0c00700
7. X. Niu, B. Tian, Q. Zhu, B. Dkhil, C. Duan, Ferroelectric polymers for neuromorphic computing. Appl. Phys. Rev. **9**, 021309 (2022). https://doi.org/10.1063/5.0073085
8. X. Hou, C. Liu, Y. Ding, L. Liu, S. Wang et al., A logic-memory transistor with the integration of visible information sensing-memory-processing. Adv. Sci. **7**, 2002072 (2020). https://doi.org/10.1002/advs.202002072
9. D. Hao, Z. Yang, J. Huang, F. Shan, Recent developments of optoelectronic synaptic devices based on metal halide perovskites. Adv. Funct. Mater. **33**, 2211467 (2023). https://doi.org/10.1002/adfm.202211467
10. J. Liao, W. Wen, J. Wu, Y. Zhou, S. Hussain et al., Van der waals ferroelectric semiconductor field effect transistor for in-memory computing. ACS Nano **17**, 6095–6102 (2023). https://doi.org/10.1021/acsnano.3c01198
11. Z.Y. He, T.Y. Wang, J.L. Meng, H. Zhu, L. Ji et al., CMOS back-end compatible memristors for *in situ* digital and neuromorphic computing applications. Mater. Horiz. **8**, 3345–3355 (2021). https://doi.org/10.1039/d1mh01257f
12. G. Wu, B. Tian, L. Liu, W. Lv, S. Wu et al., Programmable transition metal dichalcogenide homojunctions controlled by nonvolatile ferroelectric domains. Nat. Electron. **3**, 43–50 (2020). https://doi.org/10.1038/s41928-019-0350-y
13. B.B. Tian, J.L. Wang, S. Fusil, Y. Liu, X.L. Zhao et al., Tunnel electroresistance through organic ferroelectrics. Nat. Commun. **7**, 11502 (2016). https://doi.org/10.1038/ncomms11502
14. L. Shi, G. Zheng, B. Tian, B. Dkhil, C. Duan, Research progress on solutions to the sneak path issue in memristor crossbar arrays. Nanoscale Adv. **2**, 1811–1827 (2020). https://doi.org/10.1039/D0NA00100G
15. B. Tian, L. Liu, M. Yan, J. Wang, Q. Zhao et al., A robust artificial synapse based on organic ferroelectric polymer. Adv. Electron. Mater. **5**, 1800600 (2019). https://doi.org/10.1002/aelm.201800600
16. M. Le Gallo, A. Sebastian, R. Mathis, M. Manica, H. Giefers et al., Mixed-precision in-memory computing. Nat. Electron. **1**, 246–253 (2018). https://doi.org/10.1038/s41928-018-0054-8
17. G. Karunaratne, M. Le Gallo, G. Cherubini, L. Benini, A. Rahimi et al., In-memory hyperdimensional computing. Nat. Electron. **3**, 327–337 (2020). https://doi.org/10.1038/s41928-020-0410-3
18. W. Wan, R. Kubendran, C. Schaefer, S.B. Eryilmaz, W. Zhang et al., A compute-in-memory chip based on resistive random-access memory. Nature **608**, 504–512 (2022). https://doi.org/10.1038/s41586-022-04992-8
19. J.S. Vetter, S. Mittal, Opportunities for nonvolatile memory systems in extreme-scale high-performance computing. Comput. Sci. Eng. **17**, 73–82 (2015). https://doi.org/10.1109/MCSE.2015.4
20. K. Prall, Benchmarking and metrics for emerging memory, in *2017 IEEE International Memory Workshop (IMW)* (IEEE, Monterey, CA, USA, 2017), pp. 1–5
21. J.A. Rodriguez, K. Remack, K. Boku, K.R. Udayakumar, S. Aggarwal et al., Reliability properties of low-voltage ferroelectric capacitors and memory arrays. IEEE Trans. Device Mater. Relib. **4**, 436–449 (2004). https://doi.org/10.1109/tdmr.2004.837210
22. A. Chanthbouala, A. Crassous, V. Garcia, K. Bouzehouane, S. Fusil et al., Solid-state memories based on ferroelectric tunnel junctions. Nat. Nanotechnol. **7**, 101–104 (2011). https://doi.org/10.1038/nnano.2011.213

23. M.J. Lee, C.B. Lee, D. Lee, S.R. Lee, M. Chang et al., A fast, high-endurance and scalable non-volatile memory device made from asymmetric $Ta_2O_{(5-x)}/TaO_{(2-x)}$ bilayer structures. Nat. Mater. **10**, 625–630 (2011). https://doi.org/10.1038/nmat3070
24. W. Banerjee, Challenges and applications of emerging non-volatile memory devices. Electronics **9**, 1029 (2020). https://doi.org/10.3390/electronics9061029
25. Z. Luo, Z. Wang, Z. Guan, C. Ma, L. Zhao et al., High-precision and linear weight updates by subnanosecond pulses in ferroelectric tunnel junction for neuro-inspired computing. Nat. Commun. **13**, 699 (2022). https://doi.org/10.1038/s41467-022-28303-x
26. G. Wu, X. Zhang, G. Feng, J. Wang, K. Zhou et al., Ferroelectric-defined reconfigurable homojunctions for in-memory sensing and computing. Nat. Mater. **22**, 1499–1506 (2023). https://doi.org/10.1038/s41563-023-01676-0
27. G. Feng, Q. Zhu, X. Liu, L. Chen, X. Zhao et al., A ferroelectric fin diode for robust non-volatile memory. Nat. Commun. **15**, 513 (2024). https://doi.org/10.1038/s41467-024-44759-5
28. D. Wang, S. Hao, B. Dkhil, B. Tian, C. Duan, Ferroelectric materials for neuroinspired computing applications. Fundam. Res. (2023). https://doi.org/10.1016/j.fmre.2023.04.013
29. R. Berdan, T. Marukame, K. Ota, M. Yamaguchi, M. Saitoh et al., Low-power linear computation using nonlinear ferroelectric tunnel junction memristors. Nat. Electron. **3**, 259–266 (2020). https://doi.org/10.1038/s41928-020-0405-0
30. Q. Luo, Y. Cheng, J. Yang, R. Cao, H. Ma et al., A highly CMOS compatible hafnia-based ferroelectric diode. Nat. Commun. **11**, 1391 (2020). https://doi.org/10.1038/s41467-020-15159-2
31. F. Ambriz-Vargas, G. Kolhatkar, M. Broyer, A. Hadj-Youssef, R. Nouar et al., A complementary metal oxide semiconductor process-compatible ferroelectric tunnel junction. ACS Appl. Mater. Interfaces **9**, 13262–13268 (2017). https://doi.org/10.1021/acsami.6b16173
32. Z. Shen, L. Liao, Y. Zhou, K. Xiong, J. Zeng et al., Epitaxial growth and phase evolution of ferroelectric La-doped HfO_2 films. Appl. Phys. Lett. **120**, 162904 (2022). https://doi.org/10.1063/5.0087976
33. Z. Zhao, Y.R. Chen, J.F. Wang, Y.W. Chen, J.R. Zou et al., Engineering $Hf_{0.5}Zr_{0.5}O_2$ ferroelectric/anti-ferroelectric phases with oxygen vacancy and interface energy achieving high remanent polarization and dielectric constants. IEEE Electron Device Lett. **43**, 553–556 (2022). https://doi.org/10.1109/LED.2022.3149309
34. R. Athle, A.E.O. Persson, A. Irish, H. Menon, R. Timm et al., Effects of TiN top electrode texturing on ferroelectricity in $Hf_{1-x}Zr_xO_2$. ACS Appl. Mater. Interfaces **13**, 11089–11095 (2021). https://doi.org/10.1021/acsami.1c01734
35. P.S. Ghosh, D. DeTellem, J. Ren, S. Witanachchi, S. Ma et al., Unusual properties of hydrogen-bonded ferroelectrics: the case of cobalt formate. Phys. Rev. Lett. **128**, 077601 (2022). https://doi.org/10.1103/PhysRevLett.128.077601
36. L. Hu, R. Feng, J. Wang, Z. Bai, W. Jin et al., Space-charge-stabilized ferroelectric polarization in self-oriented croconic acid films. Adv. Funct. Mater. **28**, 1705463 (2018). https://doi.org/10.1002/adfm.201705463
37. F. Mehmood, M. Hoffmann, P.D. Lomenzo, C. Richter, M. Materano et al., Bulk depolarization fields as a major contributor to the ferroelectric reliability performance in lanthanum doped $Hf_{0.5}Zr_{0.5}O_2$ capacitors. Adv. Mater. Interfaces **6**, 1901180 (2019). https://doi.org/10.1002/admi.201901180
38. J. Hayden, M.D. Hossain, Y. Xiong, K. Ferri, W. Zhu et al., Ferroelectricity in boron-substituted aluminum nitride thin films. Phys. Rev. Mater. **5**, 044412 (2021). https://doi.org/10.1103/physrevmaterials.5.044412
39. K. Ferri, S. Bachu, W. Zhu, M. Imperatore, J. Hayden et al., Ferroelectrics everywhere: ferroelectricity in magnesium substituted zinc oxide thin films. J. Appl. Phys. **130**, 044101 (2021). https://doi.org/10.1063/5.0053755
40. D. Wang, P. Wang, B. Wang, Z. Mi, Fully epitaxial ferroelectric ScGaN grown on GaN by molecular beam epitaxy. Appl. Phys. Lett. **119**, 111902 (2021). https://doi.org/10.1063/5.0060021
41. A.I. Mardare, C.C. Mardare, E. Joanni, Bottom electrode crystallization of PZT thin films for ferroelectric capacitors. J. Eur. Ceram. Soc. **25**, 735–741 (2005). https://doi.org/10.1016/j.jeurceramsoc.2003.12.031
42. G. Le Rhun, G. Poullain, R. Bouregba, G. Leclerc, Fatigue properties of oriented PZT ferroelectric thin films. J. Eur. Ceram. Soc. **25**, 2281–2284 (2005). https://doi.org/10.1016/j.jeurceramsoc.2005.03.046
43. A. Datta, D. Mukherjee, S. Witanachchi, P. Mukherjee, Hierarchically ordered nano-heterostructured PZT thin films with enhanced ferroelectric properties. Adv. Funct. Mater. **24**, 2638–2647 (2014). https://doi.org/10.1002/adfm.201303290
44. D.H. Li, E.S. Lee, H.W. Chung, S.Y. Lee, Comparison of the effect of PLT and PZT buffer layers on PZT thin films for ferroelectric materials applications. Appl. Surf. Sci. **252**, 4541–4544 (2006). https://doi.org/10.1016/j.apsusc.2005.07.133
45. K.R. Udayakumar, P.J. Schuele, J. Chen, S.B. Krupanidhi, L.E. Cross, Thickness-dependent electrical characteristics of lead zirconate titanate thin films. J. Appl. Phys. **77**, 3981–3986 (1995). https://doi.org/10.1063/1.359508
46. S. Samanta, V. Sankaranarayanan, K. Sethupathi, Band gap, piezoelectricity and temperature dependence of differential permittivity and energy storage density of PZT with different Zr/Ti ratios. Vacuum **156**, 456–462 (2018). https://doi.org/10.1016/j.vacuum.2018.08.015
47. E.M. Lee, Y. Ahn, J.Y. Son, Effects of Mn doping on $BaTiO_3$ thin films grown on highly oriented pyrolytic graphite substrates. Curr. Appl. Phys. **20**, 755–759 (2020). https://doi.org/10.1016/j.cap.2020.03.009
48. J.L. Lin, R. He, Z. Lu, Y. Lu, Z. Wang et al., Oxygen vacancy enhanced ferroelectricity in BTO: SRO nanocomposite films. Acta Mater. **199**, 9–18 (2020). https://doi.org/10.1016/j.actamat.2020.08.016

49. H.H. Wieder, Electrical behavior of barium titanatge single crystals at low temperatures. Phys. Rev. **99**, 1161–1165 (1955). https://doi.org/10.1103/physrev.99.1161
50. C.A.-P. de Araujo, J.D. Cuchiaro, L.D. McMillan, M.C. Scott, J.F. Scott, Fatigue-free ferroelectric capacitors with platinum electrodes. Nature **374**, 627–629 (1995). https://doi.org/10.1038/374627a0
51. J. Wang, J.B. Neaton, H. Zheng, V. Nagarajan, S.B. Ogale et al., Epitaxial $BiFeO_3$ multiferroic thin film heterostructures. Science **299**, 1719–1722 (2003). https://doi.org/10.1126/science.1080615
52. N. Wang, X. Luo, L. Han, Z. Zhang, R. Zhang et al., Structure, performance, and application of $BiFeO_3$ nanomaterials. Nano-Micro Lett. **12**, 81 (2020). https://doi.org/10.1007/s40820-020-00420-6
53. G. Catalan, J.F. Scott, Physics and applications of bismuth ferrite. Adv. Mater. **21**, 2463–2485 (2009). https://doi.org/10.1002/adma.200802849
54. M.A. Rafiq, M.E. Costa, P.M. Vilarinho, Pairing high piezoelectric coefficients, d_{33}, with high curie temperature (T_C) in lead-free (K, Na)NbO_3. ACS Appl. Mater. Interfaces **8**, 33755–33764 (2016). https://doi.org/10.1021/acsami.6b08199
55. Y. Chang, S. Poterala, Z. Yang, G.L. Messing, Enhanced electromechanical properties and temperature stability of textured $(K_{0.5}Na_{0.5})NbO_3$-based piezoelectric ceramics. J. Am. Ceram. Soc. **94**, 2494–2498 (2011). https://doi.org/10.1111/j.1551-2916.2011.04393.x
56. J. Bouaziz, P.R. Romeo, N. Baboux, B. Vilquin, Huge reduction of the wake-up effect in ferroelectric HZO thin films. ACS Appl. Electron. Mater. **1**, 1740–1745 (2019). https://doi.org/10.1021/acsaelm.9b00367
57. V. Gaddam, D. Das, S. Jeon, Insertion of HfO_2 seed/dielectric layer to the ferroelectric HZO films for heightened remanent polarization in MFM capacitors. IEEE Trans. Electron Devices **67**, 745–750 (2020). https://doi.org/10.1109/TED.2019.2961208
58. B. Liu, Y. Zhang, L. Zhang, Q. Yuan, W. Zhang et al., Excellent HZO ferroelectric thin films on flexible PET substrate. J. Alloys Compd. **919**, 165872 (2022). https://doi.org/10.1016/j.jallcom.2022.165872
59. P. Wang, D. Wang, N.M. Vu, T. Chiang, J.T. Heron et al., Fully epitaxial ferroelectric ScAlN grown by molecular beam epitaxy. Appl. Phys. Lett. **118**, 223504 (2021). https://doi.org/10.1063/5.0054539
60. M.R. Islam, N. Wolff, M. Yassine, G. Schönweger, B. Christian et al., On the exceptional temperature stability of ferroelectric $Al_{1-x}Sc_xN$ thin films. Appl. Phys. Lett. **118**, 232905 (2021). https://doi.org/10.1063/5.0053649
61. R. Guido, P.D. Lomenzo, M.R. Islam, N. Wolff, M. Gremmel et al., Thermal stability of the ferroelectric properties in 100 nm-thick $Al_{0.72}Sc_{0.28}N$. ACS Appl. Mater. Interfaces **15**, 7030–7043 (2023). https://doi.org/10.1021/acsami.2c18313
62. D. Wang, J. Zheng, P. Musavigharavi, W. Zhu, A.C. Foucher et al., Ferroelectric switching in sub-20 nm aluminum scandium nitride thin films. IEEE Electron Device Lett. **41**(12), 1774–1777 (2020). https://doi.org/10.1109/LED.2020.3034576
63. A.V. Bune, V.M. Fridkin, S. Ducharme, L.M. Blinov, S.P. Palto et al., Two-dimensional ferroelectric films. Nature **391**, 874–877 (1998). https://doi.org/10.1038/36069
64. T. Furukawa, Ferroelectric properties of vinylidene fluoride copolymers. Phase Transitions **18**, 143–211 (1989). https://doi.org/10.1080/01411598908206863
65. B.B. Tian, X.F. Bai, Y. Liu, P. Gemeiner, X.L. Zhao et al., β phase instability in poly(vinylidene fluoride/trifluoroethylene) thin films near β relaxation temperature. Appl. Phys. Lett. **106**, 092902 (2015). https://doi.org/10.1063/1.4913968
66. S. Ducharme, V.M. Fridkin, A.V. Bune, S.P. Palto, L.M. Blinov et al., Intrinsic ferroelectric coercive field. Phys. Rev. Lett. **84**, 175–178 (2000). https://doi.org/10.1103/PhysRevLett.84.175
67. W.-Q. Liao, D. Zhao, Y.-Y. Tang, Y. Zhang, P.-F. Li et al., A molecular perovskite solid solution with piezoelectricity stronger than lead zirconate titanate. Science **363**, 1206–1210 (2019). https://doi.org/10.1126/science.aav3057
68. P.-F. Li, W.-Q. Liao, Y.-Y. Tang, W. Qiao, D. Zhao et al., Organic enantiomeric high-T_c ferroelectrics. Proc. Natl. Acad. Sci. U.S.A. **116**, 5878–5885 (2019). https://doi.org/10.1073/pnas.1817866116
69. J. Valasek, Piezo-electric and allied phenomena in Rochelle salt. Phys. Rev. **17**, 475–481 (1921). https://doi.org/10.1103/physrev.17.475
70. H.-Y. Zhang, Y.-Y. Tang, P.-P. Shi, R.-G. Xiong, Toward the targeted design of molecular ferroelectrics: modifying molecular symmetries and homochirality. Acc. Chem. Res. **52**, 1928–1938 (2019). https://doi.org/10.1021/acs.accounts.8b00677
71. G. Busch, P. Scherrer, Eine neue seignette-elektrische Substanz. Naturwissenschaften **23**, 737 (1935). https://doi.org/10.1007/BF01498152
72. Q. Zhao, H. Wang, Z. Ni, J. Liu, Y. Zhen et al., Organic ferroelectric-based 1T1T random access memory cell employing a common dielectric layer overcoming the half-selection problem. Adv. Mater. **29**, 1701907 (2017). https://doi.org/10.1002/adma.201701907
73. J. Hoffman, X. Pan, J.W. Reiner, F.J. Walker, J.P. Han et al., Ferroelectric field effect transistors for memory applications. Adv. Mater. **22**, 2957–2961 (2010). https://doi.org/10.1002/adma.200904327
74. X. Qian, X. Chen, L. Zhu, Q.M. Zhang, Fluoropolymer ferroelectrics: multifunctional platform for polar-structured energy conversion. Science **380**, eadg0902 (2023). https://doi.org/10.1126/science.adg0902
75. D. Buck, *Ferroelectrics for Digital Information Storage and Switching* (Massachusetts Institute of Technology, Cambridge Digital Computer Lab., Cambridge, 1952)
76. D. Bondurant, Ferroelectronic ram memory family for critical data storage. Ferroelectrics **112**, 273–282 (1990). https://doi.org/10.1080/00150199008008233

© The authors

77. C.-U. Pinnow, T. Mikolajick, Material aspects in emerging nonvolatile memories. J. Electrochem. Soc. **151**, K13 (2004). https://doi.org/10.1149/1.1740785
78. J.-M. Koo, B.-S. Seo, S. Kim, S. Shin, J.-H. Lee et al., Fabrication of 3D trench PZT capacitors for 256Mbit FRAM device application, in *IEEE International Electron Devices Meeting, 2005. IEDM Technical Digest* (2005), pp. 340–343. https://doi.org/10.1109/IEDM.2005.1609345
79. H.P. McAdams, R. Acklin, T. Blake, X.-H. Du, J. Eliason et al., A 64-Mb embedded FRAM utilizing a 130-nm 5LM Cu/FSG logic process. IEEE J. Solid State Circuits **39**, 667–677 (2004). https://doi.org/10.1109/jssc.2004.825241
80. D.A. Tenne, A. Bruchhausen, N.D. Lanzillotti-Kimura, A. Fainstein, R.S. Katiyar et al., Probing nanoscale ferroelectricity by ultraviolet Raman spectroscopy. Science **313**, 1614–1616 (2006). https://doi.org/10.1126/science.1130306
81. V. Garcia, S. Fusil, K. Bouzehouane, S. Enouz-Vedrenne, N.D. Mathur et al., Giant tunnel electroresistance for non-destructive readout of ferroelectric states. Nature **460**, 81–84 (2009). https://doi.org/10.1038/nature08128
82. J.L. Moll, Y. Tarui, A new solid state memory resistor. IEEE Trans. Electron Devices **10**, 338 (1963). https://doi.org/10.1109/T-ED.1963.15245
83. K. Sugibuchi, Y. Kurogi, N. Endo, Ferroelectric field-effect memory device using $Bi_4Ti_3O_{12}$ film. J. Appl. Phys. **46**, 2877–2881 (1975). https://doi.org/10.1063/1.322014
84. K. Takahashi, K. Aizawa, B.-E. Park, H. Ishiwara, Thirty-day-long data retention in ferroelectric-gate field-effect transistors with HfO_2 buffer layers. Jpn. J. Appl. Phys. **44**, 6218 (2005). https://doi.org/10.1143/jjap.44.6218
85. T. Kijima, H. Matsunaga, Preparation of $Bi_4Ti_3O_{12}$ thin films by MOCVD method and electrical properties of metal/ferroelectric/insulator/semiconductor structure. Jpn. J. Appl. Phys. **38**, 2281 (1999). https://doi.org/10.1143/jjap.38.2281
86. S. Sakai, R. Ilangovan, Metal-ferroelectric-insulator-semiconductor memory FET with long retention and high endurance. IEEE Electron Device Lett. **25**, 369–371 (2004). https://doi.org/10.1109/LED.2004.828992
87. M. Si, A.K. Saha, S. Gao, G. Qiu, J. Qin et al., A ferroelectric semiconductor field-effect transistor. Nat. Electron. **2**, 580–586 (2019). https://doi.org/10.1038/s41928-019-0338-7
88. U. Schroeder, M.H. Park, T. Mikolajick, C.S. Hwang, The fundamentals and applications of ferroelectric HfO_2. Nat. Rev. Mater. **7**, 653–669 (2022). https://doi.org/10.1038/s41578-022-00431-2
89. J. Park, T.-H. Kim, O. Kwon, M. Ismail, C. Mahata et al., Implementation of convolutional neural network and 8-bit reservoir computing in CMOS compatible VRRAM. Nano Energy **104**, 107886 (2022). https://doi.org/10.1016/j.nanoen.2022.107886
90. T.S. Böscke, J. Müller, D. Bräuhaus, U. Schröder, U. Böttger, Ferroelectricity in hafnium oxide: CMOS compatible ferroelectric field effect transistors, in *2011 International Electron Devices Meeting* (IEEE, Washington, DC, USA, 2011), pp. 24.5.1–24.5.4
91. S. Fujii, Y. Kamimuta, T. Ino, Y. Nakasaki, R. Takaishi et al., First demonstration and performance improvement of ferroelectric HfO_2-based resistive switch with low operation current and intrinsic diode property, in *2016 IEEE Symposium on VLSI Technology* (IEEE, Honolulu, HI, USA, 2016), pp. 1–2
92. J. Okuno, T. Kunihiro, K. Konishi, H. Maemura, Y. Shuto et al., SoC compatible 1T1C FeRAM memory array based on ferroelectric $Hf_{0.5}Zr_{0.5}O_2$, in *2020 IEEE Symposium on VLSI Technology* (IEEE, Honolulu, HI, USA, 2020), pp. 1–2
93. J. Yang, Q. Luo, X. Xue, H. Jiang, Q. Wu et al., A 9Mb HZO-based embedded FeRAM with 1012-cycle endurance and 5/7ns read/write using ECC-assisted data refresh and offset-canceled sense amplifier, in *2023 IEEE International Solid-State Circuits Conference (ISSCC)* (IEEE, San Francisco, CA, USA, 2023), pp. 1–3
94. M.H. Park, C.-C. Chung, T. Schenk, C. Richter, K. Opsomer et al., Effect of annealing ferroelectric HfO_2 thin films: *in situ*, high temperature X-ray diffraction. Adv. Electron. Mater. **4**, 1800091 (2018). https://doi.org/10.1002/aelm.201800091
95. Y. Goh, J. Hwang, Y. Lee, M. Kim, S. Jeon, Ultra-thin $Hf_{0.5}Zr_{0.5}O_2$ thin-film-based ferroelectric tunnel junction via stress induced crystallization. Appl. Phys. Lett. **117**, 242901 (2020). https://doi.org/10.1063/5.0029516
96. R. Materlik, C. Künneth, A. Kersch, The origin of ferroelectricity in $Hf_{1-x}Zr_xO_2$: a computational investigation and a surface energy model. J. Appl. Phys. **117**, 134109 (2015). https://doi.org/10.1063/1.4916707
97. Y. Wei, P. Nukala, M. Salverda, S. Matzen, H.J. Zhao et al., A rhombohedral ferroelectric phase in epitaxially strained $Hf_{0.5}Zr_{0.5}O_2$ thin films. Nat. Mater. **17**, 1095–1100 (2018). https://doi.org/10.1038/s41563-018-0196-0
98. T. Mikolajick, S. Slesazeck, H. Mulaosmanovic, M.H. Park, S. Fichtner et al., Next generation ferroelectric materials for semiconductor process integration and their applications. J. Appl. Phys. **129**, 100901 (2021). https://doi.org/10.1063/5.0037617
99. S. Fichtner, N. Wolff, F. Lofink, L. Kienle, B. Wagner, AlScN: a III-V semiconductor based ferroelectric. J. Appl. Phys. **125**, 114103 (2019). https://doi.org/10.1063/1.5084945
100. K. Yazawa, A. Zakutayev, G.L. Brennecka, A Landau–Devonshire analysis of strain effects on ferroelectric $Al_{1-x}Sc_xN$. Appl. Phys. Lett. **121**, 042902 (2022). https://doi.org/10.1063/5.0098979
101. R. Mizutani, S. Yasuoka, T. Shiraishi, T. Shimizu, M. Uehara et al., Thickness scaling of $(Al_{0.8}Sc_{0.2})N$ films with remanent polarization beyond 100 μC cm^{-2} around 10 nm in thickness. Appl. Phys. Express **14**, 105501 (2021). https://doi.org/10.35848/1882-0786/ac2261
102. D. Drury, K. Yazawa, A. Zakutayev, B. Hanrahan, G. Brennecka, High-temperature ferroelectric behavior of $Al_{0.7}Sc_{0.3}N$. Micromachines **13**, 887 (2022). https://doi.org/10.3390/mi13060887

103. W. Zhu, J. Hayden, F. He, J.-I. Yang, P. Tipsawat et al., Strongly temperature dependent ferroelectric switching in AlN, $Al_{1-x}Sc_xN$, and $Al_{1-x}BxN$ thin films. Appl. Phys. Lett. **119**, 062901 (2021). https://doi.org/10.1063/5.0057869
104. D. Wang, P. Wang, S. Mondal, M. Hu, D. Wang et al., Thickness scaling down to 5 nm of ferroelectric ScAlN on CMOS compatible molybdenum grown by molecular beam epitaxy. Appl. Phys. Lett. **122**, 052101 (2023). https://doi.org/10.1063/5.0136265
105. J.X. Zheng, M.M.A. Fiagbenu, G. Esteves, P. Musavigharavi, A. Gunda et al., Ferroelectric behavior of sputter deposited $Al_{0.72}Sc_{0.28}N$ approaching 5 nm thickness. Appl. Phys. Lett. **122**, 222901 (2023). https://doi.org/10.1063/5.0147224
106. G. Schönweger, N. Wolff, M.R. Islam, M. Gremmel, A. Petraru et al., In-grain ferroelectric switching in sub-5 nm thin $Al_{0.74}$ $Sc_{0.26}$ N films at 1 V. Adv. Sci. **10**, e2302296 (2023). https://doi.org/10.1002/advs.202302296
107. G. Schönweger, M.R. Islam, N. Wolff, A. Petraru, L. Kienle et al., Ultrathin $Al_{1-x}Sc_xN$ for low-voltage-driven ferroelectric-based devices. Phys. Status Solidi RRL **17**, 2200312 (2023). https://doi.org/10.1002/pssr.202200312
108. W. Sun, J. Zhou, N. Liu, S. Zheng, X. Li et al., Integration of ferroelectric $Al_{0.8}Sc_{0.2}N$ on Si (001) substrate. IEEE Electron Device Lett. **45**, 574–577 (2024). https://doi.org/10.1109/LED.2024.3363724
109. D. Wang, P. Wang, S. Mondal, S. Mohanty, T. Ma et al., An epitaxial ferroelectric ScAlN/GaN heterostructure memory. Adv. Electron. Mater. **8**, 2200005 (2022). https://doi.org/10.1002/aelm.202200005
110. N. Farrer, L. Bellaiche, Properties of hexagonal ScN versus wurtzite GaN and InN. Phys. Rev. B **66**, 201203 (2002). https://doi.org/10.1103/physrevb.66.201203
111. V. Ranjan, L. Bellaiche, E.J. Walter, Strained hexagonal ScN: a material with unusual structural and optical properties. Phys. Rev. Lett. **90**, 257602 (2003). https://doi.org/10.1103/PhysRevLett.90.257602
112. Y. Zhang, S. Wang, Y. Zhao, Y. Ding, Z. Zhang et al., Piezo-phototronic effect boosted catalysis in plasmonic bimetallic ZnO heterostructure with guided Fermi level alignment. Mater. Today Nano **18**, 100177 (2022). https://doi.org/10.1016/j.mtnano.2022.100177
113. W. Wu, Z.L. Wang, Piezotronics and piezo-phototronics for adaptive electronics and optoelectronics. Nat. Rev. Mater. **1**, 16031 (2016). https://doi.org/10.1038/natrevmats.2016.31
114. P. Wang, D. Wang, S. Mondal, Y. Wu, T. Ma et al., Interfacial modulated lattice-polarity-controlled epitaxy of III-nitride heterostructures on Si(111). ACS Appl. Mater. Interfaces **14**, 15747–15755 (2022). https://doi.org/10.1021/acsami.1c23381
115. P. Muralt, R.G. Polcawich, S. Trolier-McKinstry, Piezoelectric thin films for sensors, actuators, and energy harvesting. MRS Bull. **34**, 658–664 (2009). https://doi.org/10.1557/mrs2009.177
116. S. Zhang, D. Holec, W.Y. Fu, C.J. Humphreys, M.A. Moram, Tunable optoelectronic and ferroelectric properties in Sc-based III-nitrides. J. Appl. Phys. **114**, 133510 (2013). https://doi.org/10.1063/1.4824179
117. J. Cai, N. Chen, Microscopic mechanism of the wurtzite-to-rocksalt phase transition of the group-III nitrides from first principles. Phys. Rev. B **75**, 134109 (2007). https://doi.org/10.1103/physrevb.75.134109
118. H. Vollstädt, E. Ito, M. Akaishi, S. Akimoto et al., High pressure synthesis of Rocksalt type of AlN. Proc. Jpn. Acad. B-Phys. **66**(1), 7–9 (1990). https://doi.org/10.2183/pjab.66.7
119. J. Zagorac, D. Zagorac, M. Rosić, J.C. Schön, B. Matović, Structure prediction of aluminum nitride combining data mining and quantum mechanics. CrystEngComm **19**, 5259–5268 (2017). https://doi.org/10.1039/C7CE01039G
120. M. Durandurdu, Pressure-induced phase transition in AlN: an *ab initio* molecular dynamics study. J. Alloys Compd. **480**, 917–921 (2009). https://doi.org/10.1016/j.jallcom.2009.02.060
121. A.M. Saitta, F. Decremps, Unifying description of the wurtzite-to-rocksalt phase transition in wide-gap semiconductors: the effect of d electrons on the elastic constants. Phys. Rev. B **70**, 035214 (2004). https://doi.org/10.1103/physrevb.70.035214
122. F. Tasnádi, B. Alling, C. Höglund, G. Wingqvist, J. Birch et al., Origin of the anomalous piezoelectric response in wurtzite $Sc_xAl_{1-x}N$ alloys. Phys. Rev. Lett. **104**, 137601 (2010). https://doi.org/10.1103/PhysRevLett.104.137601
123. H. Wang, N. Adamski, S. Mu, C.G. Van de Walle, Piezoelectric effect and polarization switching in $Al_{1-x}Sc_xN$. J. Appl. Phys. **130**, 104101 (2021). https://doi.org/10.1063/5.0056485
124. M. Akiyama, T. Kamohara, K. Kano, A. Teshigahara, Y. Takeuchi et al., Enhancement of piezoelectric response in scandium aluminum nitride alloy thin films prepared by dual reactive cosputtering. Adv. Mater. **21**, 593–596 (2009). https://doi.org/10.1002/adma.200802611
125. T. Yanagitani, M. Suzuki, Electromechanical coupling and gigahertz elastic properties of ScAlN films near phase boundary. Appl. Phys. Lett. **105**, 122907 (2014). https://doi.org/10.1063/1.4896262
126. S. Yasuoka, T. Shimizu, A. Tateyama, M. Uehara, H. Yamada et al., Effects of deposition conditions on the ferroelectric properties of $(Al_{1-x}Sc_x)N$ thin films. J. Appl. Phys. **128**, 114103 (2020). https://doi.org/10.1063/5.0015281
127. G. Schönweger, A. Petraru, M.R. Islam, N. Wolff, B. Haas et al., From fully strained to relaxed: epitaxial ferroelectric $Al_{1-x}Sc_xN$ for III-N technology. Adv. Funct. Mater. **32**, 2109632 (2022). https://doi.org/10.1002/adfm.202109632
128. P. Wang, D. Wang, Y. Bi, B. Wang, J. Schwartz et al., Quaternary alloy ScAlGaN: a promising strategy to improve the quality of ScAlN. Appl. Phys. Lett. **120**, 012104 (2022). https://doi.org/10.1063/5.0060608
129. J. Casamento, H. Lee, T. Maeda, V. Gund, K. Nomoto et al., Epitaxial $Sc_xAl_{1-x}N$ on GaN exhibits attractive high-K

© The authors

dielectric properties. Appl. Phys. Lett. **120**, 152901 (2022). https://doi.org/10.1063/5.0075636

130. S.-L. Tsai, T. Hoshii, H. Wakabayashi, K. Tsutsui, T.-K. Chung et al., Publisher's Note: "Room-temperature deposition of a poling-free ferroelectric AlScN film by reactive sputtering." Appl. Phys. Lett. **118**, 082902 (2021). https://doi.org/10.1063/5.0035335
131. K. Yazawa, D. Drury, A. Zakutayev, G.L. Brennecka, Reduced coercive field in epitaxial thin film of ferroelectric wurtzite $Al_{0.7}Sc_{0.3}N$. Appl. Phys. Lett. **118**, 162903 (2021). https://doi.org/10.1063/5.0043613
132. H. Moriwake, R. Yokoi, A. Taguchi, T. Ogawa, C.A.J. Fisher et al., A computational search for wurtzite-structured ferroelectrics with low coercive voltages. APL Mater. **8**, 121102 (2020). https://doi.org/10.1063/5.0023626
133. S. Yasuoka, R. Mizutani, R. Ota, T. Shiraishi, T. Shimizu et al., Enhancement of crystal anisotropy and ferroelectricity by decreasing thickness in (Al, Sc)N films. J. Ceram. Soc. Japan **130**, 436–441 (2022). https://doi.org/10.2109/jcersj2.21184
134. S. Fichtner, F. Lofink, B. Wagner, G. Schönweger, T.-N. Kreutzer et al., Ferroelectricity in AlScN: switching, imprint and sub-150 nm films, in *2020 Joint Conference of the IEEE International Frequency Control Symposium and International Symposium on Applications of Ferroelectrics (IFCS-ISAF)* (IEEE, Keystone, CO, USA, 2020), pp. 1–4
135. S.K. Ryoo, K.D. Kim, H.W. Park, Y.B. Lee, S.H. Lee et al., Investigation of optimum deposition conditions of radio frequency reactive magnetron sputtering of $Al_{0.7}Sc_{0.3}N$ film with thickness down to 20 nm. Adv. Electron. Mater. **8**, 2200726 (2022). https://doi.org/10.1002/aelm.202200726
136. S. Rassay, F. Hakim, C. Li, C. Forgey, N. Choudhary et al., A segmented-target sputtering process for growth of sub-50 nm ferroelectric scandium–aluminum–nitride films with composition and stress tuning. Phys. Status Solidi RRL **15**, 2100087 (2021). https://doi.org/10.1002/pssr.202100087
137. J. Wang, M. Park, A. Ansari, High-temperature acoustic and electric characterization of ferroelectric $Al_{0.7}Sc_{0.3}N$ films. J. Microelectromech. Syst. **31**, 234–240 (2022). https://doi.org/10.1109/JMEMS.2022.3147492
138. V. Gund, B. Davaji, H. Lee, M.J. Asadi, J. Casamento et al., Temperature-dependent lowering of coercive field in 300 nm sputtered ferroelectric $Al_{0.70}Sc_{0.30}N$, in *2021 IEEE International Symposium on Applications of Ferroelectrics (ISAF)* (IEEE, Sydney, Australia, 2021), pp. 1–3
139. D. Drury, K. Yazawa, A. Mis, K. Talley, A. Zakutayev et al., Understanding reproducibility of sputter-deposited metastable ferroelectric wurtzite $Al_{0.6}Sc_{0.4}N$ films using in situ optical emission spectrometry. Phys. Status Solidi RRL **15**, 2100043 (2021). https://doi.org/10.1002/pssr.202100043
140. P. Chandra, M. Dawber, P.B. Littlewood, J.F. Scott, Scaling of the coercive field with thickness in thin-film ferroelectrics. Ferroelectrics **313**, 7–13 (2004). https://doi.org/10.1080/00150190490891157
141. K.-H. Kim, I. Karpov, R.H. Olsson, D. Jariwala, Wurtzite and fluorite ferroelectric materials for electronic memory. Nat. Nanotechnol. **18**, 422–441 (2023). https://doi.org/10.1038/s41565-023-01361-y
142. H. Lu, G. Schönweger, A. Petraru, H. Kohlstedt, S. Fichtner et al., Domain dynamics and resistive switching in ferroelectric $Al_{1-x}Sc_xN$ thin film capacitors. Adv. Funct. Mater. (2024). https://doi.org/10.1002/adfm.202315169
143. D.H. Lee, Y. Lee, Y.H. Cho, H. Choi, S.H. Kim et al., Unveiled ferroelectricity in well-known non-ferroelectric materials and their semiconductor applications. Adv. Funct. Mater. **33**, 2303956 (2023). https://doi.org/10.1002/adfm.202303956
144. H. Huyan, L. Li, C. Addiego, W. Gao, X. Pan, Structures and electronic properties of domain walls in $BiFeO_3$ thin films. Natl. Sci. Rev. **6**, 669–683 (2019). https://doi.org/10.1093/nsr/nwz101
145. X. Zhang, E.A. Stach, W.J. Meng, A.C. Meng, Nanoscale compositional segregation in epitaxial AlScN on Si (111). Nanoscale Horiz. **8**, 674–684 (2023). https://doi.org/10.1039/d2nh00567k
146. X. Zhang, W. Xu, W.J. Meng, A.C. Meng, Single crystal ferroelectric AlScN nanowires. CrystEngComm **26**, 180–191 (2024). https://doi.org/10.1039/d3ce00990d
147. K. Do Kim, Y.B. Lee, S.H. Lee, I.S. Lee, S.K. Ryoo et al., Evolution of the ferroelectric properties of AlScN film by electrical cycling with an inhomogeneous field distribution. Adv. Electron. Mater. **9**, 2201142 (2023). https://doi.org/10.1002/aelm.202201142
148. N. Wolff, S. Fichtner, B. Haas, M.R. Islam, F. Niekiel et al., Atomic scale confirmation of ferroelectric polarization inversion in wurtzite-type AlScN. J. Appl. Phys. **129**, 034103 (2021). https://doi.org/10.1063/5.0033205
149. P. Visconti, D. Huang, M.A. Reshchikov, F. Yun, R. Cingolani et al., Investigation of defects and surface polarity in GaN using hot wet etching together with microscopy and diffraction techniques. Mater. Sci. Eng. B **93**, 229–233 (2002). https://doi.org/10.1016/S0921-5107(02)00011-9
150. D. Zhuang, J.H. Edgar, Wet etching of GaN, AlN, and SiC: a review. Mater. Sci. Eng. R. Rep. **48**, 1–46 (2005). https://doi.org/10.1016/j.mser.2004.11.002
151. S. Calderon 5th., J. Hayden, S.M. Baksa, W. Tzou, S. Trolier-McKinstry et al., Atomic-scale polarization switching in wurtzite ferroelectrics. Science **380**, 1034–1038 (2023). https://doi.org/10.1126/science.adh7670
152. J. Lao, M. Yan, B. Tian, C. Jiang, C. Luo et al., Ultralow-power machine vision with self-powered sensor reservoir. Adv. Sci. **9**, e2106092 (2022). https://doi.org/10.1002/advs.202106092
153. S.M. Rossnagel, Magnetron sputtering. J. Vac. Sci. Technol. A Vac. Surf. Films **38**, 060805 (2020). https://doi.org/10.1116/6.0000594
154. V. Yoshioka, J. Lu, Z. Tang, J. Jin, R.H. Olsson III. et al., Strongly enhanced second-order optical nonlinearity in CMOS-compatible $Al_{1-x}Sc_xN$ thin films. APL Mater. **9**, 101104 (2021). https://doi.org/10.1063/5.0061787

155. O. Ambacher, B. Christian, N. Feil, D. Urban, C. Elsässer et al., Wurtzite ScAlN, InAlN, and GaAlN crystals, a comparison of structural, elastic, dielectric, and piezoelectric properties. J. Appl. Phys. **130**, 045102 (2021). https://doi.org/10.1063/5.0048647
156. M. Akiyama, K. Kano, A. Teshigahara, Influence of growth temperature and scandium concentration on piezoelectric response of scandium aluminum nitride alloy thin films. Appl. Phys. Lett. **95**, 162107 (2009). https://doi.org/10.1063/1.3251072
157. S. Yasuoka, R. Mizutani, R. Ota, T. Shiraishi, T. Shimizu et al., Tunable ferroelectric properties in wurtzite $(Al_{0.8}Sc_{0.2})N$ via crystal anisotropy. ACS Appl. Electron. Mater. **4**, 5165–5170 (2022). https://doi.org/10.1021/acsaelm.2c00999
158. X. Liu, D. Wang, K.-H. Kim, K. Katti, J. Zheng et al., Post-CMOS compatible aluminum scandium nitride/2D channel ferroelectric field-effect-transistor memory. Nano Lett. **21**, 3753–3761 (2021). https://doi.org/10.1021/acs.nanolett.0c05051
159. P. Musavigharavi, A.C. Meng, D. Wang, J. Zheng, A.C. Foucher et al., Nanoscale structural and chemical properties of ferroelectric aluminum scandium nitride thin films. J. Phys. Chem. C **125**, 14394–14400 (2021). https://doi.org/10.1021/acs.jpcc.1c01523
160. X. Liu, J. Zheng, D. Wang, P. Musavigharavi, E.A. Stach et al., Aluminum scandium nitride-based metal–ferroelectric–metal diode memory devices with high on/off ratios. Appl. Phys. Lett. **118**, 202901 (2021). https://doi.org/10.1063/5.0051940
161. D. Wang, P. Musavigharavi, J. Zheng, G. Esteves, X. Liu et al., Sub-microsecond polarization switching in (Al, Sc)N ferroelectric capacitors grown on complementary metal–oxide–semiconductor-compatible aluminum electrodes. Phys. Status Solidi RRL **15**, 2000575 (2021). https://doi.org/10.1002/pssr.202000575
162. S. Satoh, K. Ohtaka, T. Shimatsu, S. Tanaka, Crystal structure deformation and phase transition of AlScN thin films in whole Sc concentration range. J. Appl. Phys. **132**, 025103 (2022). https://doi.org/10.1063/5.0087505
163. X. Liu, J. Ting, Y. He, M.M.A. Fiagbenu, J. Zheng et al., Reconfigurable compute-In-memory on field-programmable ferroelectric diodes. Nano Lett. **22**, 7690–7698 (2022). https://doi.org/10.1021/acs.nanolett.2c03169
164. S.R.C. McMitchell, A.M. Walke, K. Banerjee, S. Mertens, X. Piao et al., Engineering strain and texture in ferroelectric scandium-doped aluminium nitride. ACS Appl. Electron. Mater. **5**, 858–864 (2023). https://doi.org/10.1021/acsaelm.2c01421
165. S. Yasuoka, T. Shimizu, A. Tateyama, M. Uehara, H. Yamada et al., Impact of deposition temperature on crystal structure and ferroelectric properties of $(Al_{1-x}Sc_x)N$ films prepared by sputtering method. Phys. Status Solidi A **218**, 2100302 (2021). https://doi.org/10.1002/pssa.202170049
166. D. Zhang, L. Jin, J. Li, T. Wen, C. Liu et al., MBE growth of ultra-thin GeSn film with high Sn content and its infrared/terahertz properties. J. Alloys Compd. **665**, 131–136 (2016). https://doi.org/10.1016/j.jallcom.2016.01.038
167. Z.-C. Zhang, Y. Li, J. Li, X.-D. Chen, B.-W. Yao et al., An ultrafast nonvolatile memory with low operation voltage for high-speed and low-power applications. Adv. Funct. Mater. **31**, 2102571 (2021). https://doi.org/10.1002/adfm.202102571
168. K. Frei, R. Trejo-Hernández, S. Schütt, L. Kirste, M. Prescher et al., Investigation of growth parameters for ScAlN-barrier HEMT structures by plasma-assisted MBE. Jpn. J. Appl. Phys. **58**, SC1045 (2019). https://doi.org/10.7567/1347-4065/ab124f
169. M.T. Hardy, E.N. Jin, N. Nepal, D.S. Katzer, B.P. Downey et al., Control of phase purity in high scandium fraction heteroepitaxial ScAlN grown by molecular beam epitaxy. Appl. Phys. Express **13**, 065509 (2020). https://doi.org/10.35848/1882-0786/ab916a
170. C. Yuan, M. Park, Y. Zheng, J. Shi, R. Dargis et al., Phonon heat conduction in $Al_{1-x}Sc_xN$ thin films. Mater. Today Phys. **21**, 100498 (2021). https://doi.org/10.1016/j.mtphys.2021.100498
171. Y. Zheng, J. Wang, M. Park, P. Wang, D. Wang et al., High-order sezawa mode AlScN/GaN/sapphire surface acoustic wave resonators, in *2022 IEEE 35th International Conference on Micro Electro Mechanical Systems Conference (MEMS)* (IEEE, Tokyo, Japan, 2022), pp. 1046–1049
172. J. Casamento, C.S. Chang, Y.-T. Shao, J. Wright, D.A. Muller et al., Structural and piezoelectric properties of ultra-thin $Sc_xAl_{1-x}N$ films grown on GaN by molecular beam epitaxy. Appl. Phys. Lett. **117**, 112101 (2020). https://doi.org/10.1063/5.0013943
173. M. Park, Z. Hao, R. Dargis, A. Clark, A. Ansari, Epitaxial aluminum scandium nitride super high frequency acoustic resonators. J. Microelectromech. Syst. **29**, 490–498 (2020). https://doi.org/10.1109/JMEMS.2020.3001233
174. P. Wang, D.A. Laleyan, A. Pandey, Y. Sun, Z. Mi, Molecular beam epitaxy and characterization of wurtzite $Sc_xAl_{1-x}N$. Appl. Phys. Lett. **116**, 151903 (2020). https://doi.org/10.1063/5.0002445
175. P. Wang, D. Wang, S. Mondal, Z. Mi, Ferroelectric N-polar ScAlN/GaN heterostructures grown by molecular beam epitaxy. Appl. Phys. Lett. **121**, 023501 (2022). https://doi.org/10.1063/5.0097117
176. C. Manz, S. Leone, L. Kirste, J. Ligl, K. Frei et al., Improved AlScN/GaN heterostructures grown by metal-organic chemical vapor deposition. Semicond. Sci. Technol. **36**, 034003 (2021). https://doi.org/10.1088/1361-6641/abd924
177. S. Leone, J. Ligl, C. Manz, L. Kirste, T. Fuchs et al., Metal-organic chemical vapor deposition of aluminum scandium nitride. Phys. Status Solidi RRL **14**, 1900535 (2020). https://doi.org/10.1002/pssr.201900535
178. C. Liu, Q. Wang, W. Yang, T. Cao, L. Chen et al., Multiscale modeling of $Al_{0.7}Sc_{0.3}N$-based FeRAM: the steep switching, leakage and selector-free array, in *2021 IEEE International Electron Devices Meeting (IEDM)* (IEEE, San Francisco, CA, USA, 2021), pp. 8.1.1–8.1.4

© The authors

179. N.D. Boscher, M. Wang, A. Perrotta, K. Heinze, M. Creatore et al., Metal-organic covalent network chemical vapor deposition for gas separation. Adv. Mater. **28**, 7479–7485 (2016). https://doi.org/10.1002/adma.201601010
180. J. Casamento, H. Lee, C.S. Chang, M.F. Besser, T. Maeda et al., Strong effect of scandium source purity on chemical and electronic properties of epitaxial $Sc_xAl_{1-x}N$/GaN heterostructures. APL Mater. **9**, 091106 (2021). https://doi.org/10.1063/5.0054522
181. L. Chen, C. Liu, M. Li, W. Song, W. Wang et al., Bipolar and unipolar cycling behavior in ferroelectric scandium-doped aluminum nitride, in *2022 IEEE International Symposium on Applications of Ferroelectrics (ISAF)* (IEEE, Tours, France, 2022), pp. 1–3
182. B.-T. Lin, W.-H. Lee, J. Shieh, M.-J. Chen, Ferroelectric AlN ultrathin films prepared by atomic layer epitaxy, *in SPIE Smart Structures + Nondestructive Evaluation. Proc SPIE 10968, Behavior and Mechanics of Multifunctional Materials XIII Denver, Colorado, USA,* vol. 10968 (2019), pp. 287–293. https://doi.org/10.1117/12.2522119
183. H.-Y. Shih, W.-H. Lee, W.-C. Kao, Y.-C. Chuang, R.-M. Lin et al., Low-temperature atomic layer epitaxy of AlN ultrathin films by layer-by-layer, *in situ* atomic layer annealing. Sci. Rep. **7**, 39717 (2017). https://doi.org/10.1038/srep39717
184. R. Guido, T. Mikolajick, U. Schroeder, P.D. Lomenzo, Role of defects in the breakdown phenomenon of $Al_{1-x}Sc_xN$: from ferroelectric to filamentary resistive switching. Nano Lett. **23**, 7213–7220 (2023). https://doi.org/10.1021/acs.nanolett.3c02351
185. T. Schenk, M. Pešić, S. Slesazeck, U. Schroeder, T. Mikolajick, Memory technology-a primer for material scientists. Rep. Prog. Phys. **83**, 086501 (2020). https://doi.org/10.1088/1361-6633/ab8f86
186. C.-X. Xue, Y.-C. Chiu, T.-W. Liu, T.-Y. Huang, J.-S. Liu et al., A CMOS-integrated compute-in-memory macro based on resistive random-access memory for AI edge devices. Nat. Electron. **4**, 81–90 (2021). https://doi.org/10.1038/s41928-020-00505-5
187. M. Lanza, A. Sebastian, W.D. Lu, M. Le Gallo, M.F. Chang et al., Memristive technologies for data storage, computation, encryption, and radio-frequency communication. Science **376**, eabj9979 (2022). https://doi.org/10.1126/science.abj9979
188. S. Deng, Z. Zhao, S. Kurinec, K. Ni, Y. Xiao et al., Overview of ferroelectric memory devices and reliability aware design optimization, in *Proceedings of the 2021 on Great Lakes Symposium on VLSI. June 22–25, 2021, Virtual Event, USA* (ACM, 2021), pp. 473–478
189. Z. Wang, W. Zhao, W. Kang, Y. Zhang, J.-O. Klein et al., Nonvolatile Boolean logic block based on ferroelectric tunnel memristor. IEEE Trans. Magn. **50**, 9100604 (2014). https://doi.org/10.1109/TMAG.2014.2329774
190. Z. Gao, W. Zhang, Q. Zhong, Y. Zheng, S. Lv et al., Giant electroresistance in hafnia-based ferroelectric tunnel junctions via enhanced polarization. Device **1**, 100004 (2023). https://doi.org/10.1016/j.device.2023.100004
191. K.-H. Kim, S. Oh, M.M.A. Fiagbenu, J. Zheng, P. Musavigharavi et al., Scalable CMOS back-end-of-line-compatible AlScN/two-dimensional channel ferroelectric field-effect transistors. Nat. Nanotechnol. **18**, 1044–1050 (2023). https://doi.org/10.1038/s41565-023-01399-y
192. X. Yin, X. Chen, M. Niemier, X.S. Hu, Ferroelectric FETs-based nonvolatile logic-in-memory circuits. IEEE Trans. Very Large Scale Integr. VLSI Syst. **27**, 159–172 (2019). https://doi.org/10.1109/TVLSI.2018.2871119
193. A. Sebastian, M. Le Gallo, R. Khaddam-Aljameh, E. Eleftheriou, Memory devices and applications for in-memory computing. Nat. Nanotechnol. **15**, 529–544 (2020). https://doi.org/10.1038/s41565-020-0655-z
194. R. Yang, In-memory computing with ferroelectrics. Nat. Electron. **3**, 237–238 (2020). https://doi.org/10.1038/s41928-020-0411-2
195. D. Ielmini, H.-S.P. Wong, In-memory computing with resistive switching devices. Nat. Electron. **1**, 333–343 (2018). https://doi.org/10.1038/s41928-018-0092-2
196. D. Wang, P. Wang, S. Mondal, M. Hu, Y. Wu et al., Ultrathin nitride ferroic memory with large ON/OFF ratios for analog in-memory computing. Adv. Mater. **35**, e2210628 (2023). https://doi.org/10.1002/adma.202210628
197. P. Wang, D. Wang, S. Mondal, M. Hu, Y. Wu et al., Ferroelectric nitride heterostructures on CMOS compatible molybdenum for synaptic memristors. ACS Appl. Mater. Interfaces **15**, 18022–18031 (2023). https://doi.org/10.1021/acsami.2c22798
198. V. Gund, B. Davaji, H. Lee, J. Casamento, H.G. Xing et al., Towards realizing the low-coercive field operation of sputtered ferroelectric $Sc_xAl_{1-x}N$, in *2021 21st International Conference on Solid-State Sensors, Actuators and Microsystems (Transducers)* (IEEE, Orlando, FL, USA, 2021), pp. 1064–1067